Modular Series-Stacked Bidirectional AC/DC Architecture
for 3-Phase Grid-Tied Applications

by

Trent N. Martin

B.S., University of Colorado, 2020

A thesis submitted to the

Faculty of the Graduate School of the

University of Colorado in partial fulfillment

of the requirements for the degree of

Master of Science

Department of Electrical & Computer Engineering

2023

Committee Members:

Prof. Dragan Maksimović, Chair

Prof. Luca Corradini

Dr. Inder K. Vedula

Martin, Trent N. (M.S., Electrical Engineering)

Modular Series-Stacked Bidirectional AC/DC Architecture for 3-Phase Grid-Tied Applications

Thesis directed by Prof. Prof. Dragan Maksimović

As the concern for climate change increases, methods to reduce greenhouse gas emissions have become a priority. The transportation sector has been identified as a major source of greenhouse gas emission and is therefore a target for improvement. Specifically, vendors have promised to replace conventional internal combustion engine vehicles (ICEs) with battery electric vehicles (BEVs/EVs) or fuel cell electric vehicles (FCEVs) in the coming decades. Such a massive paradigm shift places significant demand on the electrical grid as alternatives like hydrogen pumps and EV chargers continue to replace existing gas stations.

As the demands of systems such as power-to-hydrogen (P2H) and extreme fast charging (XFC) increase, there is a need for highly efficient, customizable, and scalable grid-tied power electronics that can be deployed rapidly. Conventional architectures that utilize line frequency transformers and low frequency buses pose many issues when it comes to efficiency, scaleability, lead times, and cost. This thesis presents a bidirectional converter architecture comprised of stackable three-phase ac/dc converter modules, scalable to high-power and high-current applications. Multiple converter modules containing a converter power stage and controls can be stacked to obtain a medium-voltage ac (MVAC) tied system without the need for a line frequency transformer. The modular system architecture is made possible by a quadruple active bridge (QAB) dc/dc converter that provides isolation between each of the three ac-side phases within each module and the dc load. The system also removes the need for bulk energy storage by taking advantage of constant balanced three-phase power flow. Decentralized module-level controllers are also implemented to allow for system modularity and scalability. The proposed architecture is validated by simulations of a P2H system consisting of 18 modules and a scaled proof-of-concept hardware prototype consisting of two modules.

Dedication

To my family.

Acknowledgements

I would like to express my appreciation towards Prof. Dragan Maksimović for providing me with excellent education and understanding of the fundamentals of Power Electronics. His assistance through lectures and through life speaks volumes to his character. His teaching will continue to impact me moving forwards.

I would also like to thank my other committee members, Prof. Luca Corradini and Dr. Inder K. Vedula in improving and enhancing this work through their guidance.

I also want to extend my gratitude to Dr. Gab-Su Seo from the National Renewable Energy Laboratory and Prof. Brian Johnson for their additional guidance and mentorship.

To Dr. Clyde Oakley, your classes in high school were what inspired me to pursue electrical engineering; I could not have done it without you.

Lastly, I am so grateful to my brothers Scott and Ryan, as well as my parents, for being with me every step of the way. Without your support, none of this would have been possible.

Contents

Chapter

Tables

Table

Figures

Figure

Chapter 1

Introduction

1.1   Motivation for Electrification of Transportation

The transportation sector is a significant contributor to the world's greenhouse gas (GHG) emissions, making it a primary target for decarbonization efforts. The work in this thesis is motivated by the ongoing movement to decarbonize the transportation sector and explores the benefits of electrification in achieving this goal. Electrification has the potential to reduce energy consumption, displace petroleum as the primary energy source, and mitigate the negative impacts of transportation on the environment. The transportation sector accounts for 28% of total US energy use, with 67% of total oil consumption in the US coming from this sector alone (Fig. 1.1,1.2). By going electric, the sector has the opportunity to replace petroleum usage with bulk energy generation, which could be fully renewable, resulting in a completely decarbonized transportation system. Moreover, transportation is responsible for 37% of GHG emissions, making it the fastest growing source of emissions (Fig 1.3). Electrification can significantly reduce these emissions, leading to improved air quality and overall quality of life in areas affected by pollution [30]. Therefore, this research seeks to explore power converter technologies that can aid in the adoption of electrified transportation to decarbonize the sector, reducing GHG emissions, and improving the environment.

Electric vehicles (EVs) and fuel cell electric vehicles (FCEVs) are capable of aiding in the decarbonization of the transportation sector due to their lack of direct emissions from the tailpipe [29].

According to a report by the International Energy Agency (IEA), the global stock of EVs

Figure 1.1: "The United States is a nation on the move. About 28% of total U.S. energy consumption in 2021 was for transporting people and goods from one place to another" [9].

Share of total U.S. energy used for transportation, 2021

transportation
28%

other
72%
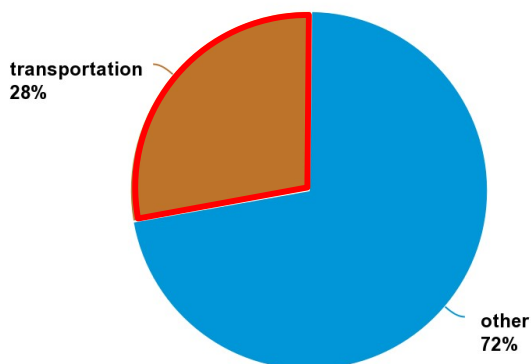
Figure 1.2: "In 2021, petroleum products accounted for about 90% of the total U.S. transportation sector energy use. Biofuels contributed about 6%. Natural gas accounted for about 4%, most of which was used in natural gas pipeline compressors. Electricity use by mass transit systems provided less than 1% of total transportation sector energy use." [9].

U.S. transportation energy sources/fuels, 2021 1

natural gas
4%

biofuels
5%

other3
3%

jet fuel (petroleum)
11%

gasoline (petroleum)2
54%

distillates (petroleum)2
23%
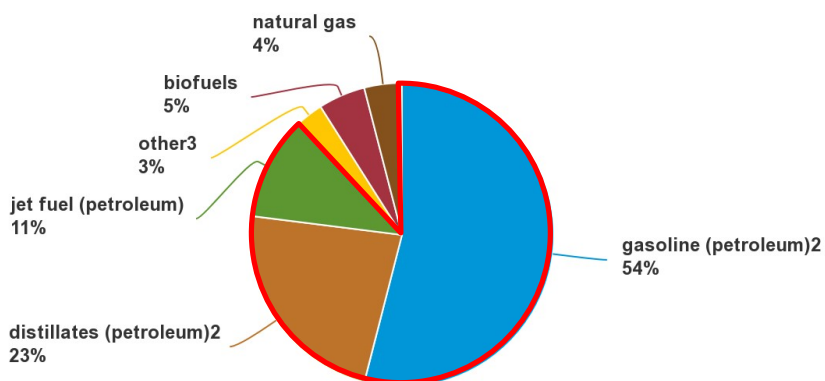
reached 10 million in 2020. The report estimates that the number of EVs on the road could increase

to 145 million by 2030, potentially reducing global CO2 emissions by 1.5 gigatons (Gt) per year [29].

Similarly, a study conducted by the National Renewable Energy Laboratory (NREL) concluded

that FCEVs could reduce GHG emissions by up to 80% compared to conventional vehicles when

Figure 1.3: "Consumption of fossil fuels accounts for most of the CO2 emissions of the major energy consuming sectors... ...the transportation sector emitted [the most] CO2 because of its near complete dependence on petroleum fuels", 2021 [10].

U.S. CO$_2$ emissions from energy consumption by source and sector, 2021
billion metric tons (Bmt) of carbon dioxide (CO$_2$)
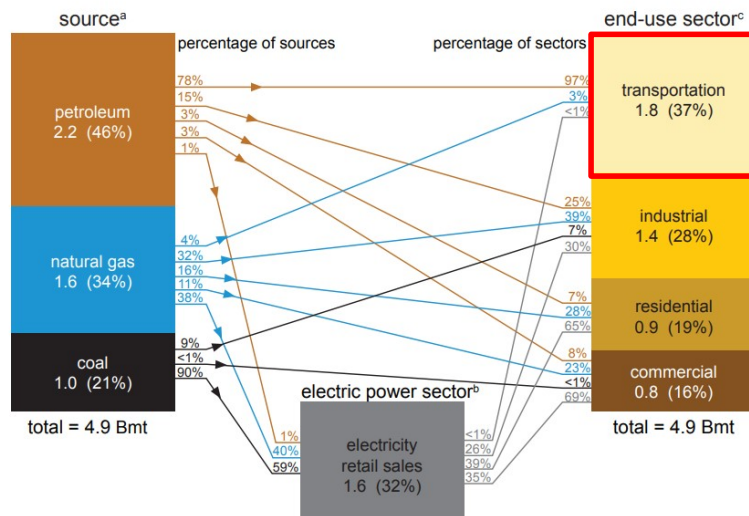
hydrogen is produced from renewable sources [18].

While electrification of the transportation sector through alternative offers significant benefits in reducing GHG emissions, it does not fully address the decarbonization challenge. Although direct emissions from the tailpipe are eliminated, there are still emissions associated with well-to-wheel emissions through grid generation (Fig. 1.4) and cradle-to-grave emissions associated with vehicle manufacturing and recycling/disposal. Therefore, it is essential to consider the source of energy for EVs and FCEVs. In both national and local contexts, the grid depends on energy sources that emit GHGs, with natural gas being the largest contributor nationally and coal being the largest in Colorado. It can be noted that petroleum contributes almost nothing to the electricity generation of the US. Based on the current energy mix in the US, a single EV generates approximately 2817 lbs of CO2 emissions annually, while in Colorado, this number increases to 3813 lbs of CO2 (Fig. 1.5). However, it is important to note that about 20% of electricity generation in the US comes from renewable sources, and there is a growing trend towards renewable generation due to economic incentives and pressures (Fig. 1.6).

Figure 1.4: "Total emissions include both tailpipe and upstream emissions. The total emissions rate is affected by a vehicle's efficiency (MPG and/or MPGe), the fuel or fuels used to power the vehicle (electricity and/or gasoline), and how that fuel is produced and distributed" [1]
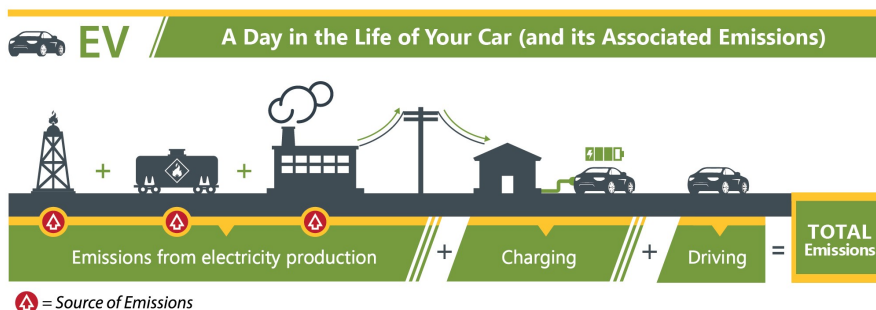
Figure 1.5: "All-electric vehicles and PHEVs running only on electricity have zero tailpipe emissions, but electricity production, such as power plants, may generate emissions." [19]
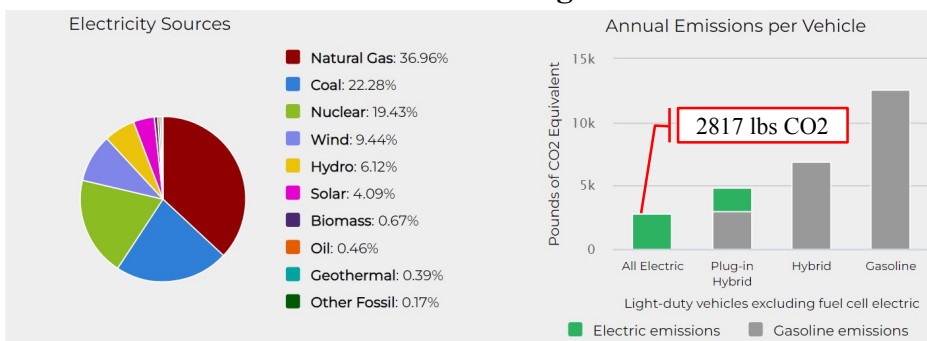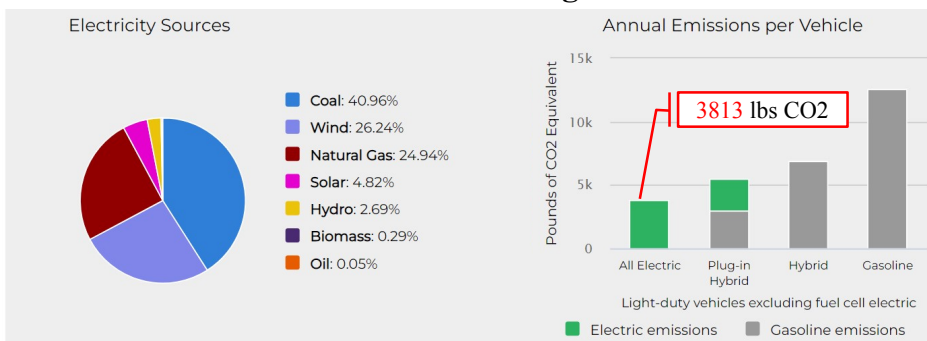
Figure 1.6:   "Renewable energy sources provide an increasing share of U.S. electricity Many renewable energy sources are used to generate electricity and were the source of about 20% of total U.S. electricity generation in 2021", 1960-2021 [14]
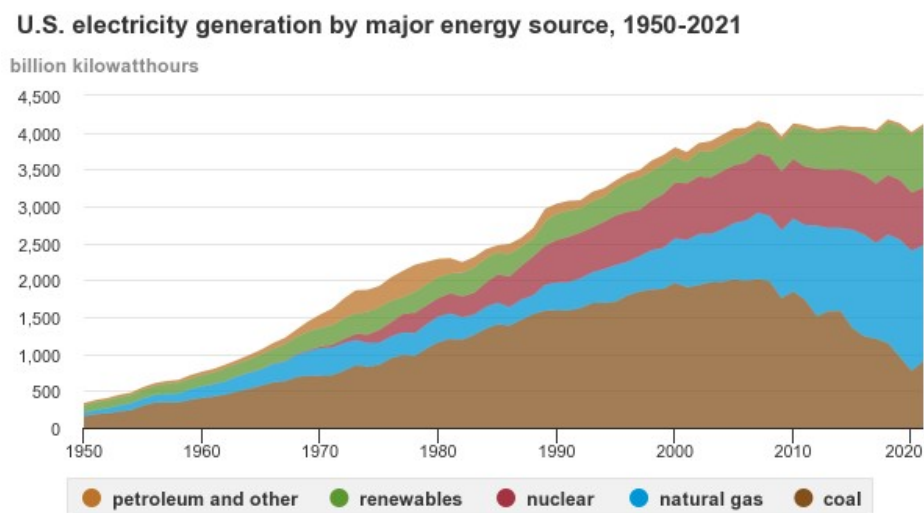
1.2   EVs and ICEs, a Comparison

Let us now compare the advantages and disadvantages of internal combustion vehicles and electric vehicles. A comparison of two Volkswagen mid-class vehicles can be found in Fig. 1.7 and will be the focus of this section.

Regenerative braking provides an advantage to EVs as it allows the vehicle to convert the energy generated during braking, which would have been lost as waste heat in an ICE, into electrical energy that can be stored in the battery [41]. This process reduces the amount of energy that is wasted during braking and increases the vehicle's efficiency as compared to an ICE vehicle. The regenerative braking system in an EV works by using an electric traction motor to slow down the vehicle when the driver steps on the brake pedal. The motor acts as a generator and converts the kinetic energy of the moving vehicle into electrical energy that can be stored in the battery. This stored energy can then be used to power the vehicle and extend its range. In contrast, a conventional ICE vehicle uses friction brakes to slow down the vehicle, which generates a significant amount of heat that is lost to the environment. This energy loss reduces the efficiency of the vehicle and

Figure 1.7: Comparison of an EV and ICE mid-class vehicle from Volkswagen. [6, 4]

	2023 VW Taos (ICE)	2023 VW ID.4 (EV)
Regenerative Braking	NO	YES
Tank-to-Wheel Efficiency	≈ 20% 1.1 kWh/mi, 31 mpg	≈ 85% 0.31 kWh/mi, 107 mpg equiv.
Energy Storage	Gasoline energy content 12.3 kWh/kg, 33.7 kWh/gal	LiFePO4 battery 0.1 kWh/kg, 0.8 kWh/gal
Refueling	5 gal/min 11 MW, 8400 mi/hr	Level I (120Vac): 1.5 kW, <8 mi/ hr Level II (240Vac): 6 kW, <32 mi/hr Level III (DC): 100 kW, <540 mi/ hr
Fuel Cost	11 ¢/mi [$3.46/gal]	4.4 ¢/mi [$0.14/kWh]
CO_2 Emissions (tailpipe, total)	(286, 346) g CO2/mi	(0, ≈130) g CO2/mi [current U.S. electricity mix]

increases its fuel consumption.

Improvements in tank-to-wheel efficiency is an additional key advantage of EVs over ICE vehicles. The efficiency of the drivetrain in an EV is much higher than that of an ICE, due to the inherently more efficient design of an electric motor and the use of advanced power electronics [35]. Power electronics, which are a key component of the EV drivetrain, can achieve efficiencies greater than 90%, while ICEs are limited to efficiencies below 30% [16]. This means that a much larger percentage of the energy stored in the battery of an EV is actually used to power the vehicle's movement, resulting in a much higher tank-to-wheel efficiency. For example, the new Volkswagen Taos, which is an ICE, has an estimated fuel economy of 34 miles per gallon (mpg) in combined city/highway driving, while the Volkswagen ID.4, which is an EV, has an estimated efficiency of 107 miles per gallon equivalent (mpge) [6, 4]. This significant difference in efficiency is due to the more efficient drivetrain of the ID.4, which is able to convert a higher percentage of the energy stored in its battery into forward motion. This efficiency advantage is expected to become even more pronounced as battery technology continues to improve and the energy grid shifts towards

cleaner and more renewable sources of power.

It is important to note that While EVs have several advantages over ICEs, one of the major limitations of EVs is their energy storage capacity. Currently, the energy density of batteries used in EVs is significantly lower than that of gasoline used in ICEs [40, 43]. This results in limited driving range for EVs compared to ICEs, which can travel longer distances on a single tank of fuel.

Another advantage of ICEs over EVs is the time it takes to refuel. Refueling an ICE vehicle with gasoline takes approximately 5 minutes, whereas recharging an EV battery can take several hours or more depending on the charging method and battery size [15, 33]. This can cause range anxiety for EV drivers who may be hesitant to take long trips or travel in areas with limited charging infrastructure.

The cost of fuel is a significant factor that affects the overall cost of ownership and operation of a vehicle. One of the main advantages of EVs over ICE vehicles is the lower cost of fuel. According to a report by the US Department of Energy, the cost of fuel for an EV is about half that of an ICE vehicle on a per-mile basis. This is mainly due to the lower cost of electricity compared to gasoline. As of 2021, the average cost of electricity in the US is around 14 cents per kilowatt-hour (kWh) [2], while the average price of gasoline is around $3.46 per gallon [11]. Based on these figures, the cost of electricity for an EV is about 4.4 cents per mile, while the cost of gasoline for an ICE vehicle is around 11 cents per mile. This makes EVs significantly cheaper to operate than ICE vehicles, especially for high-mileage drivers. It is worth noting that the cost of electricity may vary depending on the time of day, location, and other factors. However, in general, the cost of electricity is expected to remain stable or even decrease in the future, while the cost of gasoline is likely to increase due to supply and demand factors[5, 7].

EVs also have lower emissions when compared to their ICE counterparts. When powered by renewable energy, EVs produce zero direct emissions. In contrast, internal combustion engines emit pollutants such as carbon monoxide, nitrogen oxides, and particulate matter that contribute to air pollution, smog, and respiratory problems. A study conducted by the Union of Concerned Scientists (UCS) compared the emissions from EVs and gasoline-powered vehicles on a life cycle

basis, taking into account the emissions associated with vehicle manufacturing, fuel production, and vehicle operation [39]. The study found that EVs produce less than half the emissions of comparable ICEs, even when factoring in the emissions associated with battery manufacturing. The Volkswagen ID.4, for instance, emits 0 g CO2/mi in the ideal case where generation is fully renewable, and 130 g CO2/mi when well-to-wheel emissions are taken into consideration. On the other hand, the Taos, an ICE, emits 346 g CO2/mi when well-to-wheel emissions are taken into consideration.

In addition to reducing greenhouse gas emissions, EVs can also help improve air quality in urban areas. As EVs produce no tailpipe emissions, they do not contribute to local air pollution [39]. This can have significant health benefits for people living in urban areas, where air pollution levels can be high due to heavy traffic.

In summary, EVs offer several benefits over ICEs, including regenerative braking, higher efficiency from tank to wheel, lower fuel costs, and reduced emissions. However, one of the major limitations of EVs is their energy storage capacity, which results in limited driving range. Additionally, refueling an EV battery takes significantly longer than refueling an ICE vehicle with gasoline, which can cause range anxiety. Despite these limitations, EVs are expected to become more popular as battery technology continues to improve and the energy grid shifts towards cleaner and more renewable sources of power.

1.3   Impediments to EV adoption

While EVs have several advantages over ICEs, such as regenerative braking, higher tank-to-wheel efficiency, lower cost of fuel, and lower emissions, there are still a few barriers to their widespread adoption.

The first major barrier is the cost of batteries. Currently, the cost of batteries stands at around $151/kWh, contributing significantly to the higher cost of EVs as compared to ICE vehicles (Fig. 1.8). For instance, an EV with a 250-mile range requires a battery of about 64 kWh, adding around $10,000 in additional vehicle cost. However, research and development are ongoing to reduce

Figure 1.8:   The trend from the annual battery price survey conducted yearly by BloombergNEF, 2013-2022 [12]

Figure 1: Volume-weighted average lithium-ion battery pack and cell price split, 2013-2022
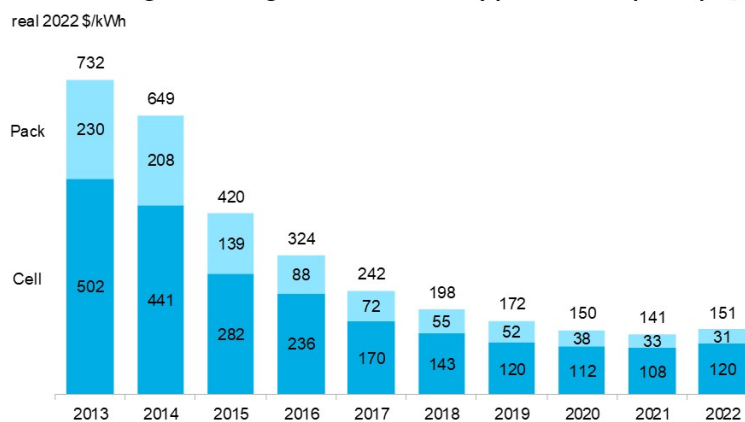
real 2022 $/kWh

Source: BloombergNEF. All values in real 2022 dollars. Weighted average survey value includes 178 data points from passenger cars, buses, commercial vehicles and stationary storage.

the cost of batteries. Battery prices are expected to drop below $100/kWh by 2026 as more lithium extraction and refining becomes available [12]. Additionally, EVs save on fuel costs, as grid energy tends to be cheaper than gasoline. Over the lifespan of the EV, the additional vehicle cost can be made up, but not by a significant amount. The reduced "Fuel" costs for grid-powered vehicles allows for savings of $1,050 over 15,000 miles of driving. This means the vehicle must be driven close to 200,000 miles, or an average lifespan of a vehicle.

EVs do provide a chance for cost reduction in the fact they are less complex than ICE-powered vehicles as they contain fewer moving parts. This reduces the need for frequent maintenance, resulting in cost savings for the vehicle owner. Maintenance costs for EVs are significantly lower than ICE vehicles, but there are uncertainties around battery life. Unfortunately, battery life is finite, and cells will eventually fail and need replacement, resulting in significant cost to the owner.

Another major impediment to EV adoption is vehicle range. The range of an EV depends on a few factors, including battery affordability, energy density, and recharge rates, all of which are ultimately limited by battery technology and cost. While day-to-day travel around town is typically not an issue as most currently available EVs can provide sufficient range for transportation around

Figure 1.9: "How Far Can You Really Drive in an Electric Vehicle? EV Range Comparison Map" [26].
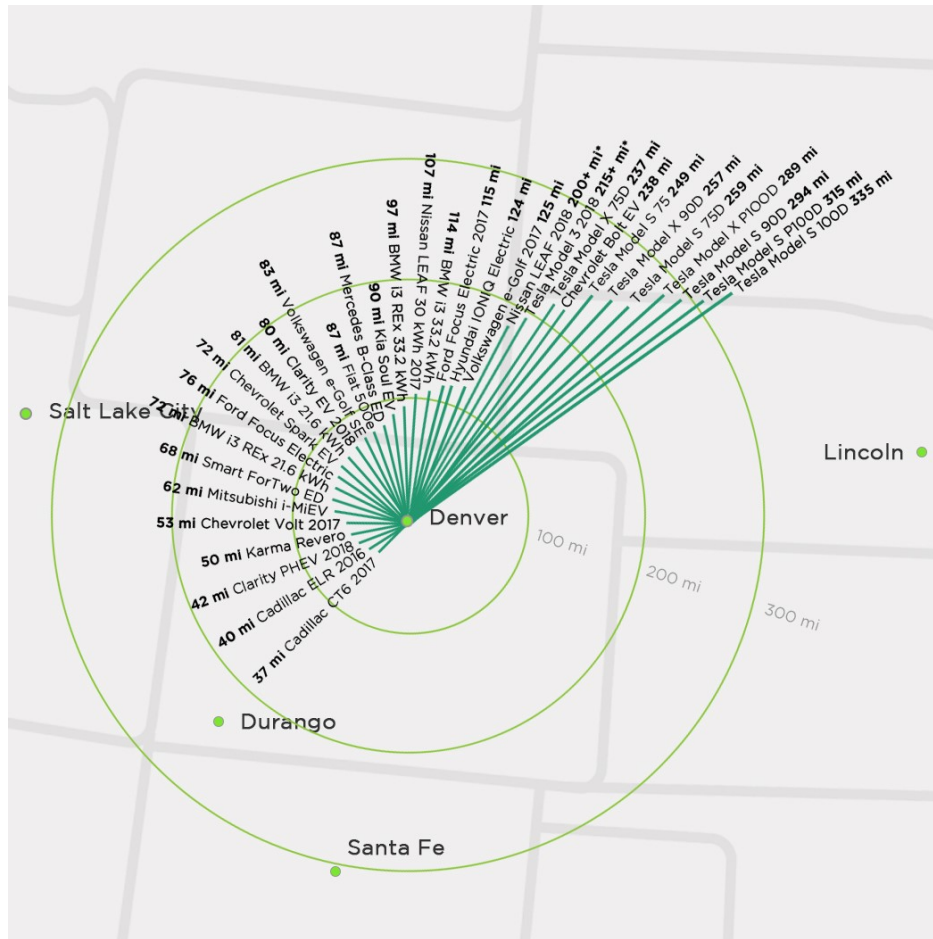
town, long-distance travel can be a challenge (Fig. 1.9). Compared to ICE vehicles, which can travel over 400 miles on a single tank of gas, the range of EVs is lacking. Currently available EVs have a range of around 335 miles on a single charge, although this varies depending on the specific model. This limited range is particularly challenging for heavy-duty freight vehicles, which are severely impacted by energy-to-weight ratios of batteries [22, 3].

The lack of charging infrastructure is another significant barrier to adoption of EVs. While public infrastructure is growing, it is still limited and not as developed as the infrastructure built for gasoline-powered vehicles. In the US, there are only around 43,000 charger locations, compared to 115,000 gas stations (Fig. 1.10). This lack of infrastructure can make it challenging for EV

Figure 1.10:   Locations of EV charging stations throught the U.S., 2021[8]

Looking for an electric vehicle charging station?

The U.S. has about 43,000 public EV charging stations and 106,000 public chargers, but they get harder to find when traveling long distances in rural areas.
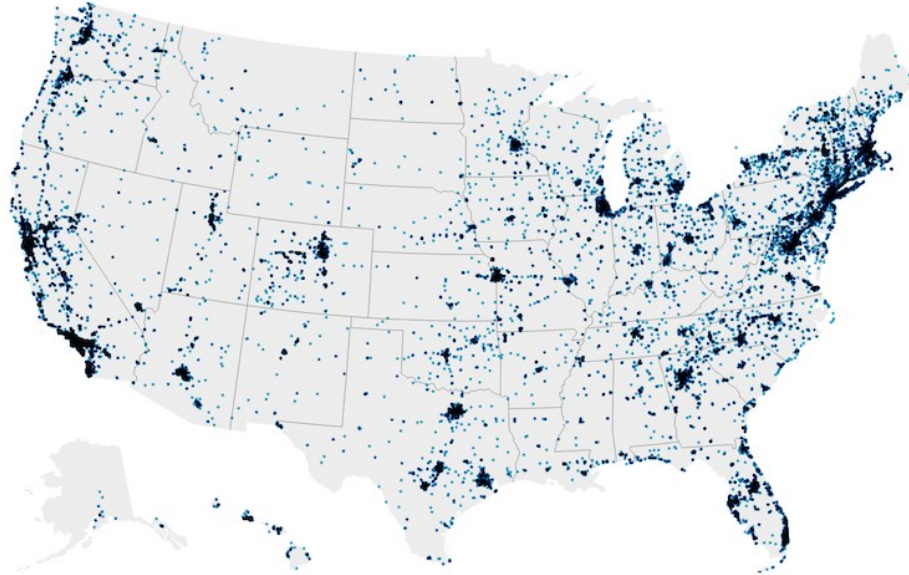
Charging stations as of August 2021. Darker areas are clusters of many stations, primarily in large cities.
Map: The Conversation/CC-BY-ND • Source: Department of Energy

drivers to find charging stations on long trips, which can create range anxiety and limit their ability to travel long distances. Additionally, high-power fast chargers, which can significantly reduce charging time, are not widely available, making it more difficult for EV drivers to quickly charge their vehicles. Currently, it can take up to an hour to add 180-240 miles worth of charge with existing chargers, which can be time-consuming and frustrating for drivers [15]. This also raises concerns about whether EV drivers will be able to make it to their destination on longer trips or whether they will have to make multiple stops to recharge. More investment is needed to expand the public charging network and develop high-power fast chargers that can quickly and conveniently charge EVs on long trips.

The adoption of EVs is a complex issue that involves a wide range of factors, including cost, range, and infrastructure. While there are still barriers to widespread adoption, it is clear that

EVs have significant advantages over ICE vehicles, including lower emissions, higher efficiency, and lower fuel costs. With continued investment and development, it is possible that EVs could become the dominant form of transportation in the coming decades.

1.4   Overview of Extreme Fast Charging

Figure 1.11:   Time to charge EV battery for different charging levels. [15]
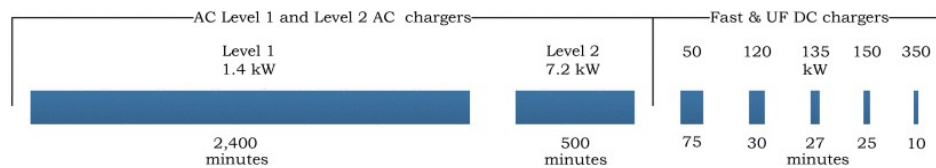
Currently available EV charger technologies include three levels: Level 1, Level 2, and DC fast chargers. Level 1 chargers are the most basic and use a standard 120-volt AC household outlet, providing up to 2.4 kW of charging power. This level of charging can take 8-12 hours to fully charge an EV, making it suitable for overnight charging. Level 2 chargers use a 240-volt AC outlet and provide up to 19.2 kW of charging power. This level of charging can charge an EV in 4-6 hours, which is suitable for home charging or workplace charging.

DC fast chargers, also known as Level 3 chargers, use direct current to provide charging power of up to 350 kW. These chargers can charge an EV from 0 to 80% in as little as 15-30 minutes, making them suitable for public charging stations and long-distance travel. However, not all EVs are compatible with DC fast charging, and the charging speed may vary depending on the specific EV model and battery capacity.

Extreme fast charging (XFC) is a type of charging technology that can charge an electric vehicle (EV) battery at a much faster rate than traditional fast chargers. XFC systems are capable of delivering power at a rate of up to 350 kW or higher, allowing EVs to charge from 0 to 80% in as little as 15 minutes. This is a significant improvement over traditional fast chargers, which typically require 30-60 minutes to charge an EV. XFC technology is still experimental and not yet

Figure 1.12: Specifications of commercially available EVs. [15]

Manufacturer	Model	Battery Specifications				Driving range per charge (Miles)	Maximum charging power (kW)
		Chemistry	Capacity (kWh)	Energy density (kWh/L)	Weight (kg)		
Volkswagen	e-golf	NMC-333	35.8	103	349	186	40
Nissan	leaf	NMC-523	62	151	410	186	50
Peugeot	e-208		50	140	356	225	100
Audi	e-torn		95	136	700	274	265
BMW	i3/i3s		42.2	152	278	246	50
Hyundai	Kona electric		67.5	149	258	484	75
Jaguar	i-pace	NMC-622	90	149	603	292	350
Kia	e-soul		64	148	457	280	77
Mercedes	EQC		85	130	652	259	110
Porsche	Taycan		93.4	148	630	280	270
Skoda	Citigo E iv		36.8	148	248	160	40
Chevrolet	Bolt EV	NMC-712	68	158	410	259	50
Renault	ZOE		54.66	168	326	239	50
Tesla	III	NCA	102.4	162	630	315	150

widely available, but has the potential to address one of the major barriers to EV adoption, which is range anxiety caused by the lack of charging infrastructure and slow charging times. By reducing charging times, XFC can make EVs more convenient and accessible to a wider range of consumers.

Many major car manufacturers have also made promises to produce fully electric vehicle lineups within the next two decades. Some examples include [17]:

(1) General Motors (GM): GM has announced plans to phase out gasoline-powered vehicles entirely by 2035, with the goal of becoming carbon-neutral by 2040.

(2) Ford: Ford has committed to investing $22 billion in electric vehicle development through 2025 and plans to sell only electric vehicles in Europe by 2030.

(3) Volkswagen (VW): VW plans to sell only electric vehicles by 2035, and the company expects EVs to make up 70% of its European sales by 2030.

(4) Volvo: Volvo plans to phase out gasoline-powered vehicles entirely by 2030 and has committed to making all its EVs available online-only.

(5) BMW: BMW plans to have 25 electric or hybrid-electric vehicles on the market by 2023 and aims to sell 7 million EVs by 2030.

(6) Toyota: Toyota plans to introduce 15 new battery-electric vehicles (BEVs) globally by 2025 and aims for half of its global sales to be electrified by 2025.

To help facilitate this transition while maintaining the expected quality of life consumers are accustomed to, chargers that can compete with gas pump fuel times need to be developed.

Figure 1.13:   Current state of the art charging technologies. [15]

Manufacturer	Model	Power (kW)	Input voltage (V)	output voltage (V)	Output current (A)	Efficiency	Time to add 200 miles
ABB	Terra 53	50	480 AC	200-500 DC 50-500 DC	120	94%	
Tritium	Veefil-RT	50	380-480 AC 600-900 DC	200-500 DC 50-500 DC	125	> 92 %	72
PHIHONG	Integrated Type	120	380 AC ± 15% 480 AC ± 15%	200-750 DC	240	93.5%	30
Tesla	Supercharger	135	380-480 AC	50-410 DC	330	91%	27
EVTEC ABB	Espresso Terra HP	150 350	400 AC ± 10%	170-500 DC 150-920 DC	300 375	93% 95%	24 10

From Fig. 1.13 it can be noted that direct medium voltage AC (MVAC) connection on the AC side is not commonly used in current EV chargers. This is because most EV chargers use low voltage AC power, which requires line-frequency transformers and low voltage distribution wiring. This leads to power losses due to the resistance of the wiring and transformers, as well as increased costs and reduced efficiency. By contrast, using direct MVAC can significantly reduce these losses and improve efficiency, which can ultimately lead to faster and more cost-effective charging for EVs.

It can also be seen that most existing EV chargers only support vehicles with lower voltage batteries in the 200 to 400V range, which is currently the norm in the market. However, newer EVs are starting to use higher voltage batteries in the 400 to 800 V range [17, 42], which can facilitate faster charging speeds. This means that existing chargers may not be able to fully take advantage of the charging capabilities of these newer EVs. To address this issue, new chargers must be designed to work with the higher voltage batteries and deliver the required power to charge them in a reasonable amount of time.

Additionally, despite the availability of fast charging technologies, most existing technology still has long charging times, usually taking 20 minutes or more to charge an EV. This is due

to limitations in the charging infrastructure and the need to balance charging speed with battery health and safety concerns[15, 42]. Addressing these limitations will require continued innovation and development in charging technology, infrastructure, and battery technology to create faster, more reliable and efficient charging solutions. By improving the charging times and expanding the range of compatible vehicles, we can make EVs a more attractive and convenient option for drivers, ultimately promoting their widespread adoption.

1.4.1   Current Trends in EV Charging

Current trends in EV charger technology are moving towards higher output power to reduce charging times and higher output voltage to support modern vehicles with higher battery voltages. For example, chargers supporting the Chaoji standard, which is a Chinese fast-charging standard, started being released in 2020. However, even with the current fast charging technologies available, charging an EV can still take significant time, highlighting the need for further innovation and development in EV charger technology.

Figure 1.14:

Standard	CHAdeMO	GB/T	CCS Type 1	CCS Type 2	Tesla	ChaoJi
Compliant Standards	IEEE 2030.1.1 IEC 62916-3	IEC 62916-3	SAE J1772 IEC 62916-3	IEC 62916-3	No related items	CHAdeMO and GB/T (IEC and CCS not yet but is ongoing)
Connector Inlet						
Maximum Voltage (V)	1000	750	600	900	500*	1500
Maximum Current (A)	400	250	400	400	631*	600
Maximum Power (kW)	400	185	200	350	250*	900
Maximum Market Power (kW)	150	125	150	350	250	N.A.
Communication Protocol	CAN		PLC		CAN	CAN
V2X Function	Yes		No		Unknown	Yes
Start year	2009	2013	2014	2013	2012	2020
Note *: The specifications of Tesla Supercharger V3 is estimated based on the label of the Tesla Supercharger V3 at Fremont. [51]						

1.4.2   Conventional MVAC-to-DC System Architectures for EV Charging

In a network of multiple chargers and local renewable energy systems, either ac or dc bus architecture can be used for connection. In the case of ac-connected systems, a step down transformer is used to interface between the distribution network and a three-phase ac bus operating at a line-to-line voltage of 250-480 V. Each charger at the station is then supplied by the ac bus, and

features a separate ac-to-dc stage. However, the increased number of conversion stages between the distribution network and the dc port of the EV or RES can lead to greater complexity, cost and decreased system efficiency. Despite this, the use of ac bus has advantages such as the availability of rectifier and inverter technology, ac switchgear and protective devices, and well-established standards for ac power distribution systems. Moreover, most advanced XFC stations are ac-connected systems, including the Tesla supercharger station in Mountain View, California, and the ABB dc fast charging station in Euroa, Victoria, Australia [42].

In the case of dc-connected systems, a single central front-end ac-to-dc converter is used to create a dc bus, which interfaces more efficiently with dc energy storage and renewable energy sources. This front-end typically features a low-frequency transformer followed by either a LV rectifier stage or a solid-state transformer (SST), which combines rectification, voltage step-down, and isolation in a single unit. The dc bus voltage is usually set to be less than $1000\,\text{V}$ to accommodate the voltage range of modern batteries, which is around 400 V. Each charger is connected to the dc bus via a dc-to-dc converter. By eliminating the individual ac-to-dc converters, the number of conversion stages is reduced, leading to improved system efficiency compared to ac-connected systems. Another advantage of the dc distribution approach is that there is a single interconnection to the utility through the central front-end, which enables load diversification resulting from varying EV battery capacities and changing charge acceptance to significantly reduce installation costs. DC systems also simplify control due to the absence of reactive power, and the single inverter interconnection with the grid simplifies islanding from and connection to the main grid.

These LV based architectures share some limitations that affect their scalability and efficiency [15, 42]. Firstly, they require bulky line-frequency MV-to-LV transformers, which add significant size and can introduce inefficiencies due to transformer losses. These transformers can also be expensive to manufacture and maintain, adding to the overall cost of the system. Secondly, LV based architectures require bulky power-distribution wiring on the LV bus. This can lead to increased resistive losses and voltage drops, reducing the overall efficiency of the system. The increased wiring also takes up more physical space and can make installation more complicated and time-consuming.

Figure 1.15:   Conventional MVAC-to-DC System Architectures [42]
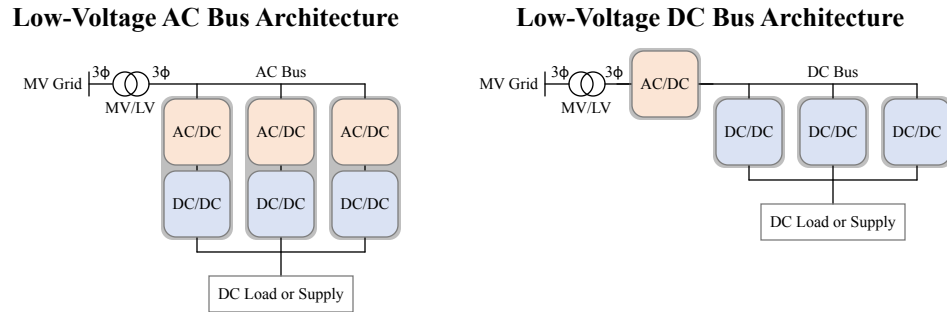
Finally, LV based architectures do not scale favorably with voltage or power. As the voltage and power levels increase, the physical size and weight of the components also increase, leading to larger and more expensive systems. alternative solutions need to be pursued to overcome these limitations and improve the efficiency and scalability of EV charger technology.

1.4.3   Modular system architectures

Modular architectures are becoming an increasingly popular alternative to traditional LV bus solutions for several reasons [15, 42]. An example of such an architecture can be seen in Fig. 1.16. One major advantage of these systems is that they are comprised of stackable LV modules capable of interfacing directly between a LV-dc and a MVAC grid. This modular design allows for greater flexibility and scalability compared to LV bus solutions. By stacking multiple modules, the overall voltage and power output can also be easily adjusted to meet the requirements of a particular application. For example, this means that modular systems can be tailored to meet the specific power and voltage needs of an EV charging station.

Another advantage of modular architectures is that they leverage high-frequency power conversion methods. This means that the components used in these systems can be relatively low-cost, low-voltage components, which can help reduce the overall cost of the system. In addition, these systems do not require a LF MV-to-LV transformer or LV power distribution wiring [28, 21, 13]. This is because the modular system converts the MVAC power directly to DC power, eliminating

Figure 1.16:

Stackable LV-HF MVAC-to-DC Modules
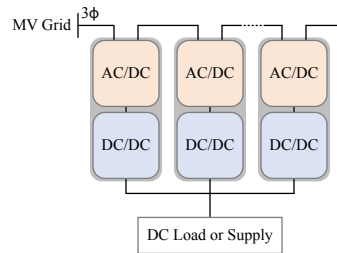
the need for these bulky components. As a result, the system can be more compact and efficient, while also being easier and less expensive to manufacture and maintain [42].

Because modular architectures utilize high-frequency power conversion methods, they also allow for more favorable voltage and power scaling. As system voltage and power levels increase, the size of components do not necessarily need to increase at the same rate as with LV bus solutions. This means that modular systems can potentially be smaller and less expensive than traditional LV bus solutions as the voltage and power levels increase. Additionally, the modular design allows for easier installation and maintenance, as individual modules can be easily replaced or upgraded without disrupting the entire system.

Overall, modular architectures are a promising alternative to traditional LV bus solutions for high-power applications like EV charging. By leveraging high-frequency power conversion methods and a modular design, these systems offer greater flexibility, scalability, and efficiency, while also potentially reducing the overall cost and size of the system.

1.5   Thesis Outline

This thesis aims to address some of the limitations of LV-based architectures for EV charging systems by presenting a novel approach utilizing a modular series stacked bidirectional MVAC-to-DC architecture.

Chapter 2 provides a comprehensive overview of the design of this architecture presented from

the system-level and module-level, detailing component selection and control loop design. By breaking the system down into modules, the architecture allows for easy scalability and flexibility in meeting various voltage and power requirements for various grid-tied applications. It then presents a system example for a power-to-hydrogen (P2H) system, which demonstrates the potential application of the modular architecture in renewable energy systems beyond EV charging. The results of the system example validate design of the module power stage and control design as well as scalability at the system level. The chapter concludes by presenting testing of a scaled 10 kW prototype. The experimental results show that the prototype achieves the desired bidirectional operation while meeting performance and efficiency, validating the viability of the modular series stacked bidirectional MVAC-to-DC architecture in hardware.

Chapter 3 concludes the paper by summarizing the thesis and its contributions and discusses potential directions for future research, such as continuation of PV inverter system integration, development of a new revision experimental prototype for P2H and XFC applications, and cost benefit analysis as compared to conventional LV based system architectures.

Chapter 2

Design of a Modular Bidirectional MVAC-to-DC Converter Architecture

2.1   Introduction

Fig. 2.1 shows a bidirectional, modular, and scalable converter architecture comprised of three single-phase ac ports and a single dc port. Three-phase ac-to-dc conversion is achieved within an individual converter module. The system is comprised of N modules where each module port can be configured to meet various application requirements. For example, three applications of the architecture are presented for PV string inverter (Fig. 2.1(a)) [13], Extreme Fast Charger (XFC)(Fig. 2.1(b)) [42, 15, 38], and Power to Hydrogen (P2H) (Fig. 2.1(c)) systems [20]. In the case of the PV string inverter, a string of PV panels is connected to each module dc port, the ac-ports are then connected in an output series configuration to interface with the MVAC grid. The XFC architecture utilizes the same series-stacked ac-port connections to facilitate MVAC grid connection, but connects the dc-ports in parallel to meet the power requirements of the electric vehicle (EV) battery. Additionally it is able to facilitate bidirectional power flow, allowing for vehicle to grid (V2G) operation of the charger. The P2H system also utilizes the series stacked ac-port connections, but uses a hybrid series-parallel connection of dc-ports to facilitate a higher dc voltage requirement while additionally meeting system power requirements.

It is possible to derive a module that can meet the flexible system requirements for the specific application. This requires a thorough understanding of the system requirements, such as voltage and power levels, efficiency, size, and cost, as well as the available components and technologies that can be used to achieve the desired performance.

Figure 2.1: Many applications have been investigated for this modular architecture. Namely, work has been conducted with NREL and the University of Washington to develop a system for PV string inverters, with the ASPIRE NSF Engineering Research Center to develop a system for XFC, and with Electric Hydrogen to develop a system for P2H.
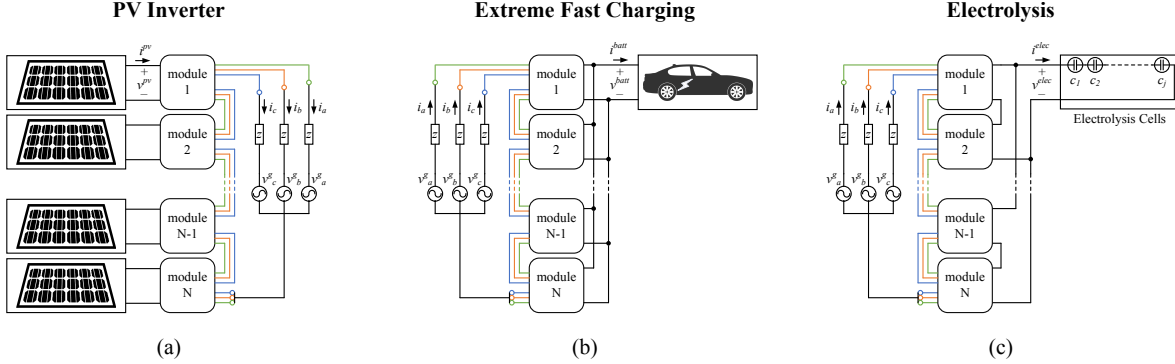

In the context of the design of a modular series stacked bidirectional MVAC-to-DC architecture, the past implementations of modular systems can provide insights into the most effective way to achieve the desired functionality and performance. By analyzing the strengths and weaknesses of past modular systems, it is possible to derive a module that can meet the specific requirements of the MVAC-to-DC architecture.

The architecture can be implemented using a modular MV converter coupled with a modular dc-dc converter via a MV dc-link, as shown in Fig. 2.2(a). In this design, several ac-to-dc modules are connected in series to interface between the MV-grid and a MV-dc bus. This is then followed by several series connected dc-to-dc modules that provide isolation between the LV-dc and MV-dc.

This can be taken a step further with the phase-modular architecture in which a single module is used to implement both the dc-to-dc stage and the MV stage. In this architecture, as seen in Fig. 2.2(b), a single module combines both the ac-to-dc conversion and the dc-to-dc conversion stages. The modules are again connected in series to form a complete system.

In the semi-modular architecture, shown in Fig. 2.2(c), instead of a single module for both the MV and DC stages, a quadruple active bridge (QAB) converter is connected to the LV side with one bridge and to one phase of the MV side with three bridges. This alteration leads to reduced

Figure 2.2: " Modular smart transformer architecture concepts: (a) architecture based on two basic building blocks (one for the MV stage, implemented using the MMC and the second for the dc-dc stage), (b) Phase modular architecture, characterized by a single building block per phase, (c) phase semi-modular architecture, also characterized by a single building block per phase, by using the semi-modular concept of dc-dc converter" [21].
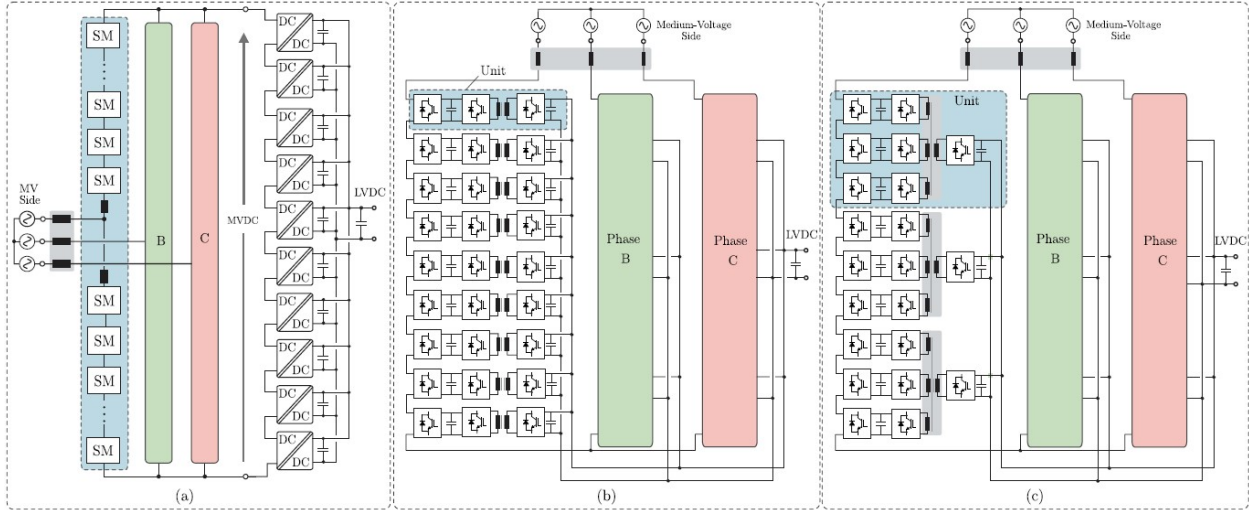
component voltage stresses, as the components in the MV stage only need to handle one-third of the total voltage.

Figure 2.3: "Interphase Modular ST Architecture" utilized in this work [21, 13].
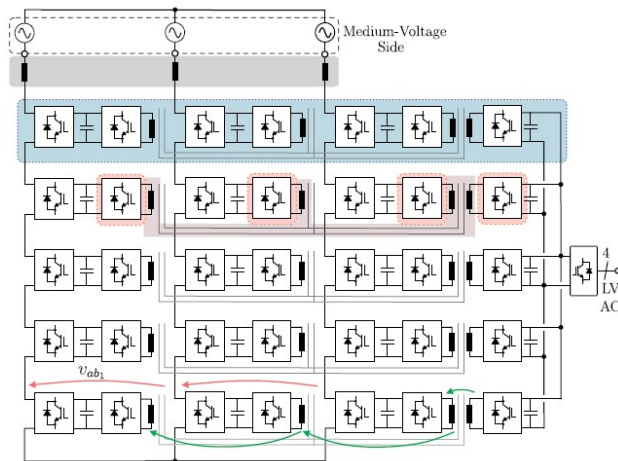
The final modular architecture, seen in Fig. 2.3, can be reached by connecting the semi-

modular architecture in an alternate configuration where each MV bridge of the QAB converter is connected to phase a, b, and c, respectively. Each phase is combined within one module, leveraging three-phase power balancing and eliminating the twice line frequency pulsating power from the dc-port. The ac-ports connected to phases a, b, and c each transfer time varying power $p_a(t)$, $p_b(t)$, and $p_c(t)$; Each contain both a dc and twice line frequency component. The three-phase powers sum, resulting in stable dc power flow through the dc-port. This relaxes the requirements of the dc-link energy storage capacitance as compared to traditional single-phase systems that require energy storage for filtering of the twice line frequency component**??**. They can be designed to filter only converter current switching ripples, reducing their sizes significantly.

Each module consists of a self-contained multi-stage three-phase ac-to-dc converter, shown in Fig. 2.4. The grid is connected to three H-bridge ac-to-dc converters that generate three separate dc-link voltages. These voltages are connected to the three primary ports of a quadruple active bridge (QAB) dc-to-dc converter. The QAB reduces power conversion stresses, improves converter efficiency, and enhances power density compared to the architecture presented in [32]. Galvanic isolation is integrated into the QAB through high-frequency transformers to facilitate a $1 : n$ winding ratio as well as module stacking. The turns ratio is selected as $1 : 1$ in all presented applications such that the QAB operates as a fixed-ratio-converter or dc-transformer (DCX). The outputs of the QAB secondaries are then interfaced with the dc side to facilitate power transfer.

In order to improve efficiencies within a module, methods for soft switching of the QAB were developed [37, 36], where the challenges are addressed related to achieving soft-switching of the dc-link bridges in the QAB converter due to power fluctuations in the ac waveform. Existing modulation strategies for soft switching in QAB converters do not fully account for device output capacitances and interactions between the magnetizing inductance and the capacitances. Reference [37] proposes a solution for achieving zero-voltage switching (ZVS) operation in the QAB stage of a converter over the entire ac line cycle by utilizing magnetizing currents of the transformers and auxiliary inductors. This is achieved by reducing the magnetizing inductance to introduce circulating currents through the secondary sides of the QAB, which greatly reduces switching loss

while slightly increasing conduction loss. The proposed solution improves efficiency and is an alternative to using a larger series inductance which reduces efficiency at full load.

Figure 2.4: Transformer-isolated ac-to-dc module using three single-phase H-bridge AC-to-DC converters, and one phase-shift controlled QAB operating in DCX. The module utilizes a distributed control scheme, allowing for each module to be controlled independently. This eliminates the need for system level control [37, 24]
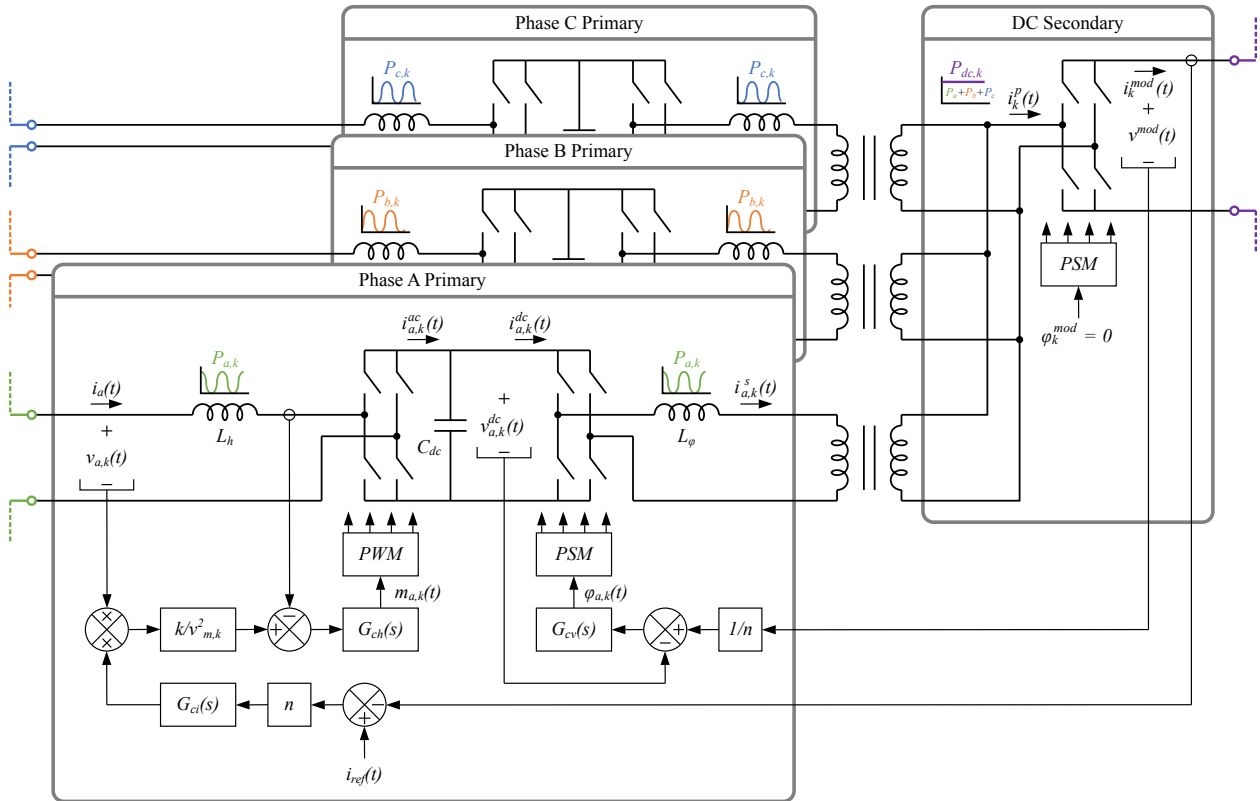
Additionally, the system takes advantage of a distributed control, meaning that each module is controlled independently rather than at the system level. To facilitate voltage regulation and power flow within one module, three control loops have been developed. An inner voltage loop regulates dc-link voltage relative to the dc-port voltage while an inner and outer current loop facilitate ac current wave-shaping at the ac-port and power flow through the module.

2.2   Design of the H-Bridge and QAB converters

In this section, we will explore the design process for the two power converter topologies within the modular converter: the H-bridge and the QAB converter. Specifically, we will detail the selection of element values and the control loop design for these converters, from the selection of key components such as inductors and capacitors, to the development on control loops.

2.2.1   Component Selection for the H-bridge converter

The analysis of the H-bridge converter (Fig. 2.5) follows that of a boost rectifier operating as a low-harmonic rectifier in continuous conduction mode (CCM) [25].

Figure 2.5:   Ac-to-dc system based on the H-bridge converter.
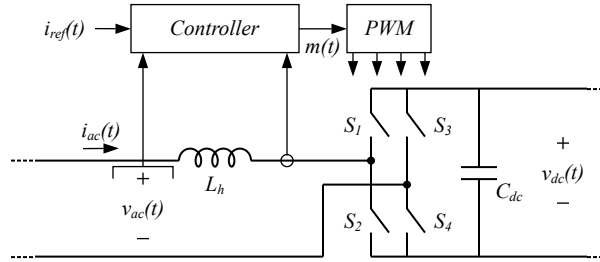
Let us first solve for the filter inductance L_h of the H-bridge converter. Ideally, the boost converter should produce an ac-line current that has the same wave-shape and phase as the ac-line voltage with very low THD. This means that the ac current should be directly proportional to the input voltage that is applied to the rectifier through an emulated resistance R_e that is varied thorough the ac-line-cycle. The resulting average power flowing through the ac-port of the converter is

$$P = \frac{V_M^2}{2R_e} \Rightarrow R_e = \frac{V_M^2}{2P} \tag{2.1}$$

where V_M is the peak ac voltage. It is preferred that the converter operates in CCM during the entire ac line cycle. As a result, the filter inductance value must be selected such that its influence on the LF components of the converter waveforms can be neglected. This allows the converter

modulation signal $m(t)$ to be expressed as

$$m(t) = 1 - \frac{v_{ac}(t)}{V_{dc}} \tag{2.2}$$

where v_{ac} is the ac-line voltage and V_{dc} is the dc-link voltage. This expression only holds true when the converter operates in CCM. This is guaranteed provided that the current ripple of the inductor L_h

$$\Delta i_{ac}(t) = \frac{v_{ac}(t)m(t)T_s}{2L_h} \tag{2.3}$$

remains smaller than the average inductor current during the H-bridge switching period T_s

$$\langle i_{ac}(t) \rangle_{T_s} = \frac{v_{ac}(t)}{R_e} \tag{2.4}$$

throughout the entire ac line cycle. Therefore, an expression for CCM operation can be given as

$$\langle i_{ac}(t) \rangle_{T_s} > \Delta i_{ac}(t) \tag{2.5}$$

Rearranging (2.5) to solve for R_e leads to the expression

$$R_e < \frac{2L_h}{T_s(1 - \frac{v_{ac}(t)}{V})} \tag{2.6}$$

Since v_{ac} varies with time, the relationship found in (2.6) may only be satisfied for part of the ac line cycle. Since $0 \leq v_{ac}(t) \leq V_M$ it can be concluded that the converter operates in CCM for the entire line cycle when

$$R_e < \frac{2L_h}{T_s} \tag{2.7}$$

Combining (2.2) and (2.7) and solving for inductance yields the final boundary condition for CCM operation of the boost rectifier

$$L_h > \frac{V_M^2 T_s}{4P} \tag{2.8}$$

Let us now solve for the dc-link capacitance C_{dc}. Since the module takes advantage of three-phase power balancing, the capacitance is only responsible for filtering the switching ripple of the H-bridge converter. The dc-voltage ripple of the rectifier is given by

$$i_{c_{dc}} = C_{dc}\frac{dv_{dc}}{dt} \Rightarrow C_{dc} = \frac{Pm(t)T_s}{V_{dc}\Delta v_{dc}} \tag{2.9}$$

where Δv_{dc} is the voltage ripple on the dc-link. The worst-case voltage ripple occurs at the peaks of the ac-line voltage $m(t) \to 1$. This results in the final expression for dc-link capacitance

$$C_{dc} = \frac{PT_s}{V_{dc}\Delta v_{dc}} \tag{2.10}$$

2.2.2   Component Selection for the QAB converter

The analysis of the QAB converter follows that of a dual active bridge (DAB) (Fig. **??**) operating with phase shift modulation and can be found in [34, 23].

Figure 2.6:   Isolated dc-to-dc system based on the DAB converter.
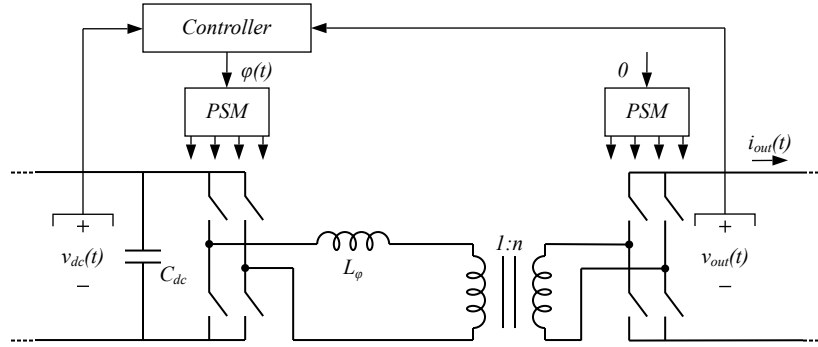
The average inductor current over the DAB switching period T_s can be found through analysis of the switching waveforms and is given as

$$\langle i_{out}(t) \rangle_{T_s} = (1 - \phi)I_{L_\phi,pk} \tag{2.11}$$

where T_s is the DAB switching period, ϕ is the PWM phase shift, and $I_{L_\phi,pk}$ is the peak inductor current defined as

$$I_{L_\phi,pk} = \frac{V_{dc}\phi T_s}{2L_\phi} \tag{2.12}$$

The voltage conversion within the DAB can also be given as

$$V_{out} = nV_{dc} \tag{2.13}$$

where V_{out} is the output voltage, n is the transformer turns ratio, and V_{dc} is the dc-link voltage. Combining (2.11), (2.12), and (2.13) results in the final expression for DAB inductance

$$L_\phi = \frac{V_{out}^2 \phi(1-\phi)T_s}{2P} \tag{2.14}$$

where P is again the average power flowing through the ac-port of the converter as found in (2.1

References [37, 36] provide a detailed analysis of zero voltage switching (ZVS) in the QAB converter, which is used in the modular architecture. Throughout an ac-line-cycle, the power that is processed by each secondary is determined by the corresponding phase shift between the secondary and the primary full bridge. By analyzing the behavior of the QAB converter and its components, [36] provides insights into how to achieve ZVS operation and improve the efficiency of the system through appropriate selection of PWM dead times. This analysis is important for ensuring that the modular architecture can operate efficiently and effectively, while also reducing component stresses and ensuring long-term reliability.

2.2.3   DC-Link Voltage Control

The primary-side QAB dc-link voltage regulation approach is illustrated in Fig. 2.7. The four QAB bridges are controlled with phase-shift modulation (PSM) where the primary and secondary side transistors are switched at a fixed 50% duty cycle and frequency f_ϕ. The rising edge of the kth module secondary-side switch signal acts as a phase reference for its three respective primaries where the phase shifts of the a-, b-, and c-side bridges are $\phi_{a,k}$, $\phi_{b,k}$, $\phi_{c,k}$, respectively.

Figure 2.7:   Dc-Link voltage control strategy consists of three identical control loops to control the dc-link of each phase relative to the dc-port voltage.
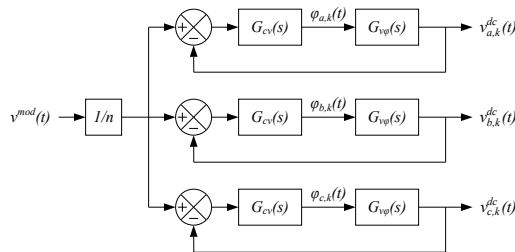
To construct a small-signal model of the QAB, each primary is treated as a separate dual active bridge (DAB) that shares the same secondary. With this assumption, the small-signal response of each DAB can be expressed as a simple first-order system [34, 23]

$$G_{v\phi}(s) = \frac{V^{dc}}{2\pi f_\phi n L_\phi C_{dc}s} \tag{2.15}$$

Where V^{dc} is the primary dc-link voltage, f_ϕ is the QAB switching frequency, n is the transformer turns ratio, L_ϕ is the QAB series inductance, and C_{dc} is the dc-link capacitance. A feedback loop with proportional-integral (PI) compensator $G_{cv(s)}$ is developed based on this model. The compensated loop generates the required phase shifts for voltage regulation of each dc link. Each QAB is controlled to operate as a fixed $1 : n$ dc transformer where the electrolyzer-stack voltage is reflected to each primary dc-link. The bandwidth of the dc-link controller is designed to be $4\,\mathrm{kHz}$, sufficiently higher than twice the line frequency, ensuring that the dc-link voltages are well regulated.

2.2.4 Current Control

As a consequence of the dc-link control strategy, the power flow from the ac to the dc side is directly tied to the grid-side control strategy. To control the power delivered to the the dc-port, average current control of the output current is implemented as shown in Fig. 2.8. To ensure autonomous power sharing among the stacking modules, it is assumed that each module provides the same partial power $P_{module} = P/N$.

Within each module, a control system includes an outer current loop designed to control the dc-port current and an inner current loop that performs ac current wave-shaping, facilitates current flow through the ac-port, and ensures that the module provides balanced three-phase power transfer. The small signal response of the boost rectifier can be expressed as [25]

$$G_{id}(s) = \frac{V^{dc}}{L_h s} \tag{2.16}$$

where V^{dc} is again the primary dc-link voltage and L_h is the series inductance of the boost rectifier.

Figure 2.8:   Current control strategy strategy consists of inner and outer current control loops.
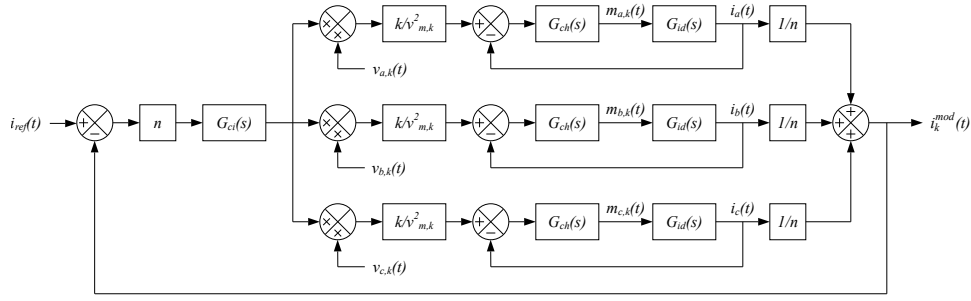
To generate the modulation required for power regulation, a feedback loop with a PI compensator $G_{ch}(s)$ is developed. The bandwidth of the inner current loop is designed to be $2\,\mathrm{kHz}$.

The outer current loop is constructed based on the outer voltage loop design principles in power factor correction rectifiers [25]. As this control loop regulates the dc current, the bandwidth is significantly lower than the line frequency. This ensures that the dc current is well regulated and unaffected by variations in load power. AS a result, converter dynamics can be neglected and a feedback loop with a PI compensator $G_{ci}(s)$ can be developed to facilitate control of the dc-port current.

Since the presented control strategies are completely self contained within one module, multiple modules can be stacked to achieve system-wide goals.

2.3   P2H System Example

This section presents an example of a Power-to-Hydrogen (P2H) system, which is a type of renewable energy system that can be used to convert excess electrical energy into hydrogen gas. The P2H system is designed using the modular architecture presented in this chapter. The system's overall operating specifications are discussed, as well as the resulting module-level design. This chapter also validates the system through simulation, including the operation of the power stage and control loops within a module and the scalability of the architecture to meet the demands of a high power MVAC tied system.

2.3.1 System and Module Level Design

A $500\,\mathrm{kW}$ P2H system connected to $13.2\,\mathrm{kV}$ MVAC with $N = 18$ modules connected as shown in Fig. 2.1(c) is considered. The operating values of the simulated system are summarized in Table 2.1. To ensure proper operation of the system at the maximum output current and to allow the use of $1200\,\mathrm{V}$ rated devices, the maximum dc voltage is selected as $v^{mod} = 800\,\mathrm{V}$. It is assumed that the electrolyzer stack is capable of absorbing the full $500\,\mathrm{kW}$ provided by the system. The H-bridge converters and QAB of each module are realized with the use of $1.2\,\mathrm{kV}$ Silicon Carbide (SiC) MOSFETs. The parameters of the simulated module are summarized in Table 2.2.

Table 2.1: Simulated system operating values.

N	No. of modules	18
n	Transformer turns ratio	$1:1$
ω	Grid frequency	$2\pi 60\,\mathrm{rad/s}$
v^g	Grid voltage	$[7.62, 7.62, 7.62]^\top \mathrm{kV}_\mathrm{rms}$
v^{mod}	Module voltage	$800\,\mathrm{V}$
v^{elec}	Electrolyzer voltage	$1.6\,\mathrm{kV}$
P	System power	$500\,\mathrm{kW}$

Table 2.2: Simulated module parameters.

f_h	H-bridge switching frequency	$10\,\mathrm{kHz}$
f_φ	QAB switching frequency	$200\,\mathrm{kHz}$
L_h	H-bridge filter inductance	$3\,\mathrm{mH}$
L_φ	QAB filter inductance	$100\,\mu\mathrm{H}$
C_{dc}	dc-link capacitance	$50\,\mu\mathrm{F}$

It is important to mention that the dc-link capacitance of each module is relatively low due to three-phase power balancing, eliminating the requirement for energy buffering. The QAB has also been designed to operate as a DCX (1:1) transformer to maximize system efficiency. Furthermore, the outputs of two modules are stacked in series to achieve a larger output voltage of $1.6\,\mathrm{kV}$.

2.3.2   Simulation Results

To verify system operation for the P2H system at $500\,\mathrm{kW}$ and $1.6\,\mathrm{kV}$, a simulation model is developed in PLECS. Fig. 2.9,2.10,2.11 shows the kth module waveforms during steady state for the case where the system supplies the electrolyzer with $500\,\mathrm{kW}$ at $1.6\,\mathrm{kV}$. The module ac voltages and currents shown in Fig. 2.9 verify that the H-bridge is generating sinusoidal ac current with high PF. Fig. 2.10 shows that balanced three-phase currents are provided to the dc-link by the H-bridge, while the properly reflected and regulated dc-link voltages are provided by the QAB. The current flow through the QAB and the resulting dc output current are also presented in Fig. 2.11. It can be concluded that the control scheme presented in Fig. 2.4 successfully regulates the dc-link, performs ac current wave-shaping, and ensures the module provides balanced three-phase power to the electrolyzer with constant dc current.

Figure 2.9:   AC waveforms from P2H simulation. Sinusoidal current generation with high PF is observed
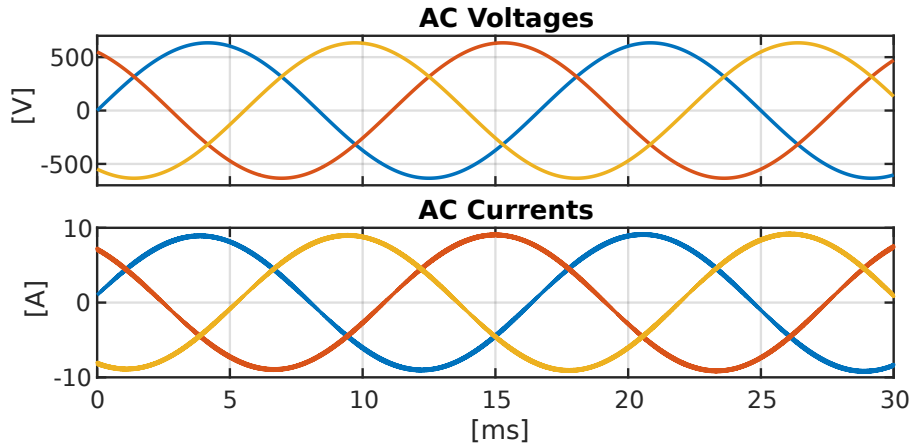
2.4   Experimental Prototype and Results

All experiments are performed with the prototype shown in Fig. 2.12, which follows the module architecture in Fig. 2.4. Each primary contains an H-bridge converter and primary leg of the QAB. The H-bridge converters and QAB of each module are realized with the use of $1.7\,\mathrm{kV}$

Figure 2.10: QAB waveforms from P2H simulation. The dc-link voltage is well regulated at 800V.
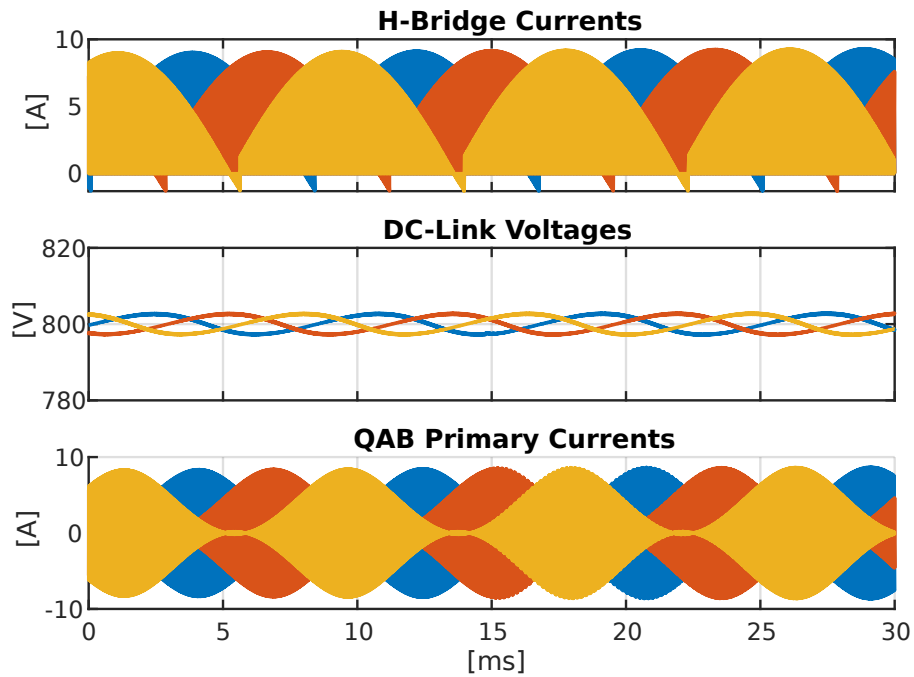

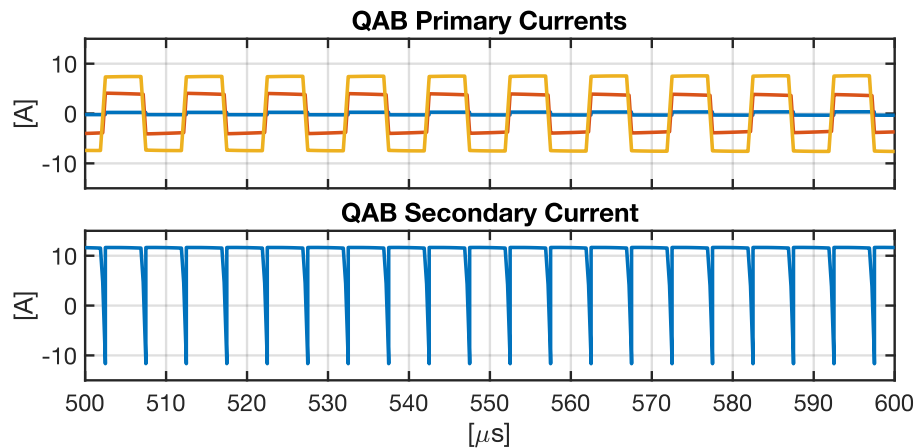Figure 2.11: Zoomed QAB waveforms from P2H simulation. 10 kW of balanced three-phase power is delivered to the load.


SiC MOSFETs. Planar magnetics capable of medium voltage isolation have also been developed for the QAB to facilitate MV isolation[37]. The secondary contains the secondary leg of the QAB and interfaces with the dc side. The operating values of the module are summarized in Table 2.3.

Table 2.3: Experimental system operating values and module parameters.

v^{mod}	Module voltage	up to $800\,\text{V}$
P	Module power	up to $10\,\text{kW}$
f_h	H-bridge switching frequency	$10-50\,\text{kHz}$
f_φ	QAB switching frequency	$200\,\text{kHz}$

The scaled prototype modules are designed to operate at up to $10\,\text{kW}$.Testing reported here has been performed at lower power and voltage levels to validate distributed control strategies for two cases. The first case details testing done to validate dc-to-ac inverter operation while the second details testing done to validate ac-to-dc rectifier operation.

Figure 2.12: A Single $10\,\text{kW}$ Module [37].
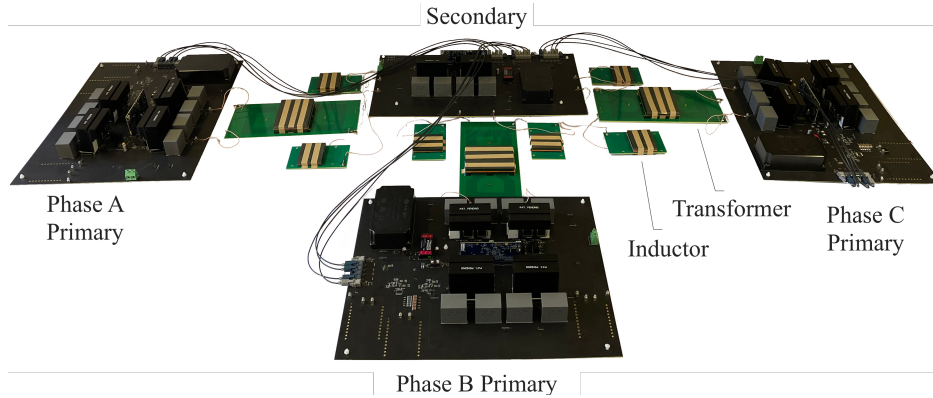
2.4.1 DC-to-AC Testing

To validate dc-to-ac inverter operation, as is the case in PV or V2G systems, tests have been conducted on a prototype shown in Fig. 2.13 and 2.14 consisting of four modules in IPOS configuration.

Fig. 2.15 shows the generated grid voltages during steady-state operation for a $132\,\Omega$ ac load for system (a) comprised of a single module and (b), comprised of the four IPOS modules. PWM interleaving from [24] has been implemented on the inverter power stage to reduce switching ripple and improve ac waveforms though module stacking. It can be seen that the interleaving successfully

Figure 2.13:   A four module system consisting of IPOS connected 10 kW modules.
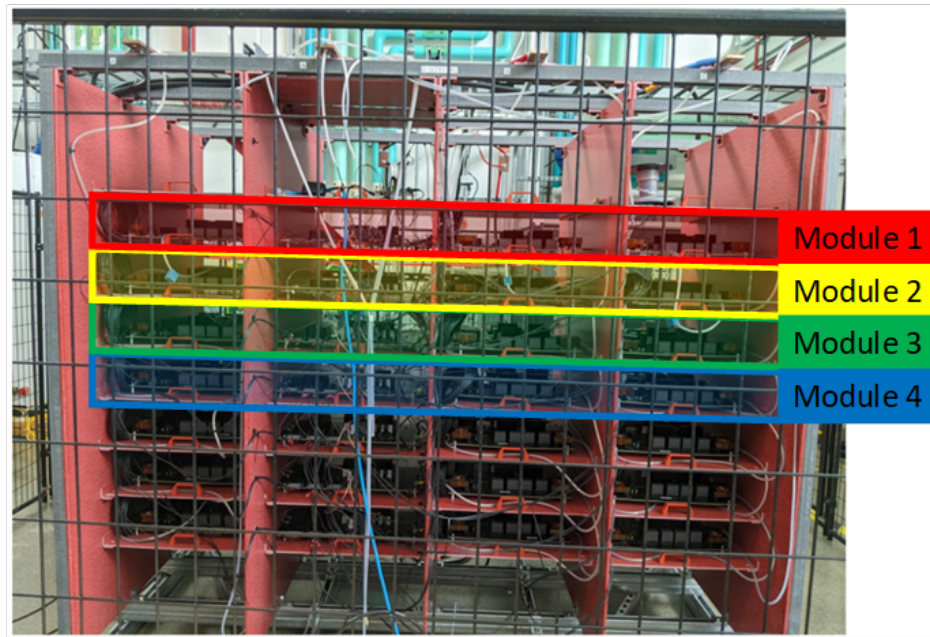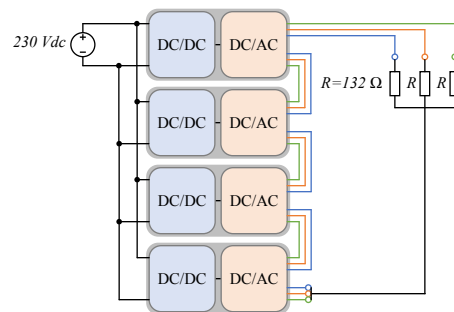

Figure 2.14:   A system with four modules in IPOS configuration for dc-to-ac testing.

reduces the ripple component in the ac voltage waveform.

Fig. 2.16 shows the generated grid voltages and currents by the four module system where the load is supplied with low power at low dc voltage, demonstrating successful balancing of three-phase power among the modules. It can be seen that a ripple component is present on the measured current. This is due to a hardware issue found in the micro-controller used for modulation of the H-bridge and QAB power stages. In order to ensure proper PWM interleaving, each module is synchronized to the others to ensure proper phase shifting. However, due to a documented

Figure 2.15: Ac-to-dc test showing voltage waveforms generated by a system comprised of a single module (a) and a system comprised of four IPOS modules (b).

(a)   (b)
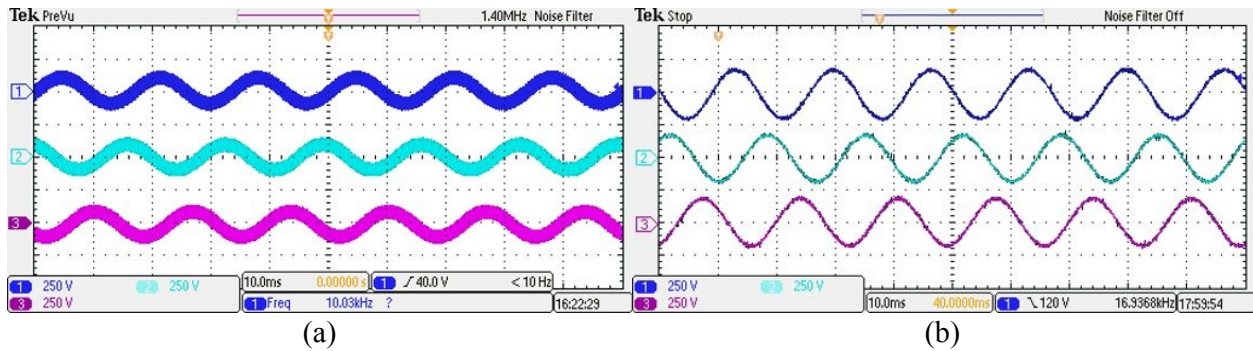
issue in the F2837xD EPWM submodule, an external synchronization event occasionally causes a discontinuity in the PWM carrier that can potentially lead to compare events between the carrier and modulation signal being skipped [31]. This results in unpredictable instability in the converter and leads to improper operation such as increase in PWM ripple in the ac current.

Figure 2.16: Ac-to-dc test showing voltage (a) and current waveforms (b) generated by a system comprised of four IPOS modules.

(a)   (b)
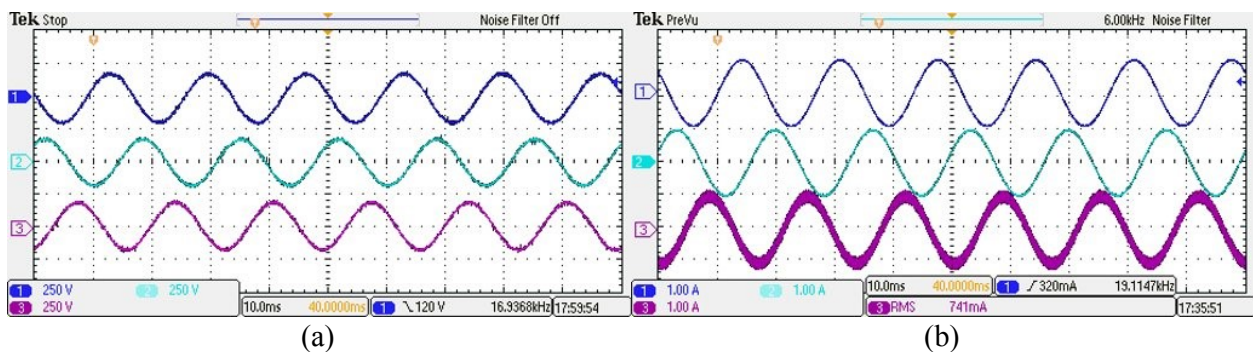
2.4.2   AC-to-DC Testing

To validate ac-to-dc rectifier operation, as is the case in XFC or P2H systems, of the system shown in Fig. 2.12 and 2.17 comprising one module attached to a $132\,\Omega$ dc load.

Fig. 2.18 shows grid voltages (a) and ac currents (b) provided to the dc load during steady-

Figure 2.17:   A system with a single module for ac-to-dc testing.

state operation where the load is supplied with low voltage and power, demonstrating that the

current control successfully generates ac current and that balanced three phase power is delivered.

Figure 2.18:   Ac-to-dc test showing voltage (a) and current waveforms (b) generated by a system comprised of a single module.

(a)   (b)
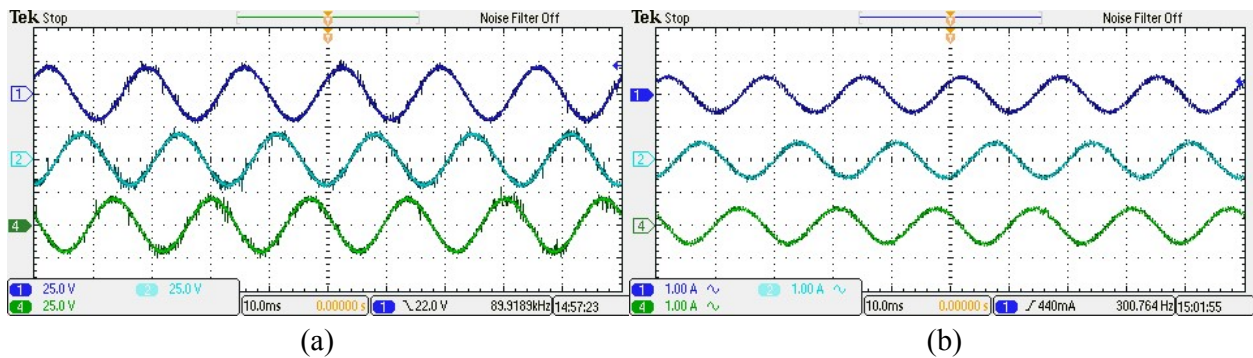
An additional test was conducted to verify operation of dc-link regulation. The results can

be seen in Fig. 2.16(a) and it can be seen that the dc-link voltage is well regulated to the dc-port

voltage of 200 V. However it can be seen in Fig. 2.16(b) that the PWM synchronization issue

previously found in the H-bridge is again found in the QAB. The improper switching results in an

extended period that causes instability in the QAB current waveform introducing oscillations into

the system.

2.4.3   ZVS operation of the QAB

ZVS operation of the QAB primary bridges also needed to be verified before testing of system

efficiencies. Fig. 2.20 shows the switch-node voltages of the QAB in a single module, demonstrating

ZVS operation throughout the operating range, most importantly at ac zero crossings. ZVS has

been validated to occur in both ac-to-dc and dc-to-ac testing.

Figure 2.19: QAB current (channel 1), switch node voltages (channels 2 and 3), and dc-link voltage (channel 4) during normal operation are shown in (a). QAB primary sync signal (channel 1), current (channel 2), and switch node voltages (channels 3 and 4) during sync issue are shown in (b).
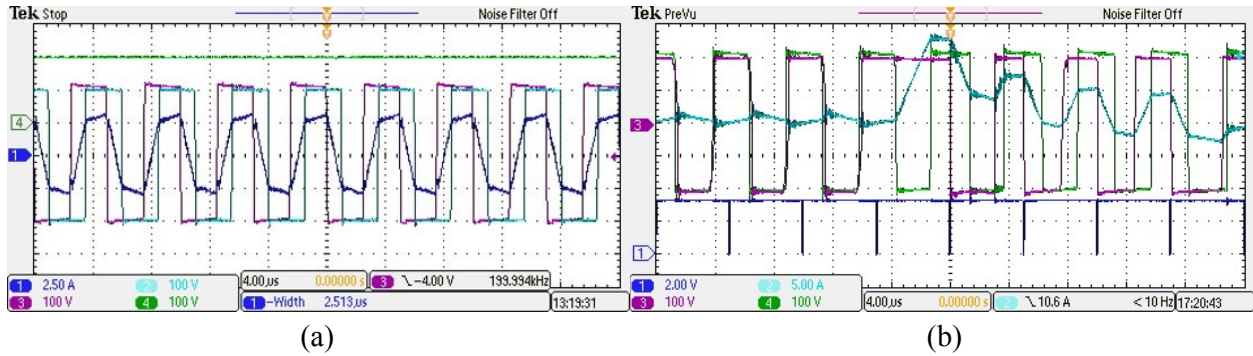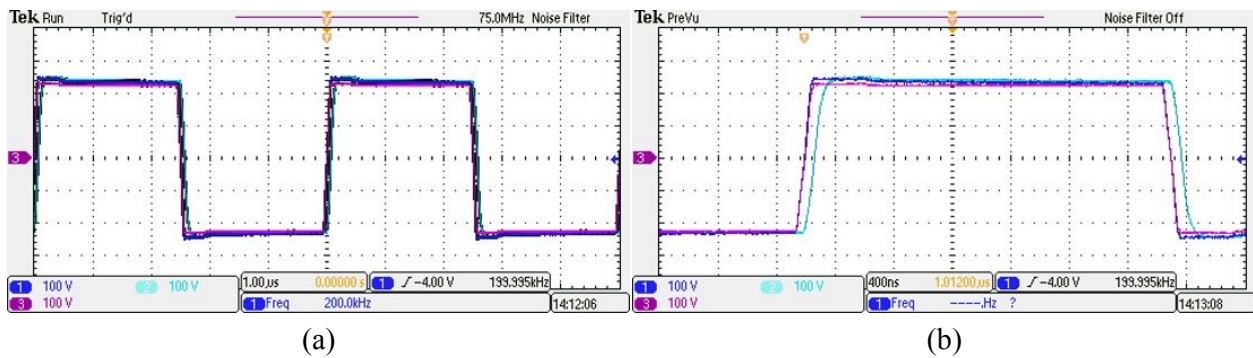

(a)   (b)

Figure 2.20: QAB primary switch node voltages at different time scales validating ZVS operation.

(a)   (b)

2.4.4 Module Loss Analysis

It was also desired to characterize the losses in a single module. Initial loss characterization was performed for a converter model at $500\,\mathrm{V}$ during ZVS operation [37, 36]. Fig. 2.21 compares the measured efficiency of the prototype when it takes advantage of ZVS operation as compared to conventional hard-switching. It can be seen that ZVS enhances system efficiency considerably as compared to the hard-switching converter.

Modeling was then performed at the full rated voltage of $1\,\mathrm{kV}$ during ZVS operation. Fig. 2.22(a) shows that the module achieves peak efficiency of %97 near $4\,\mathrm{kW}$ power throughput. Investigating further, it is found in Fig. 2.22(b) that there are three major sources of loss in the module. The first

Figure 2.21: Measured efficiency of the prototype as compared to the conventional non ZVS design [37, 36].
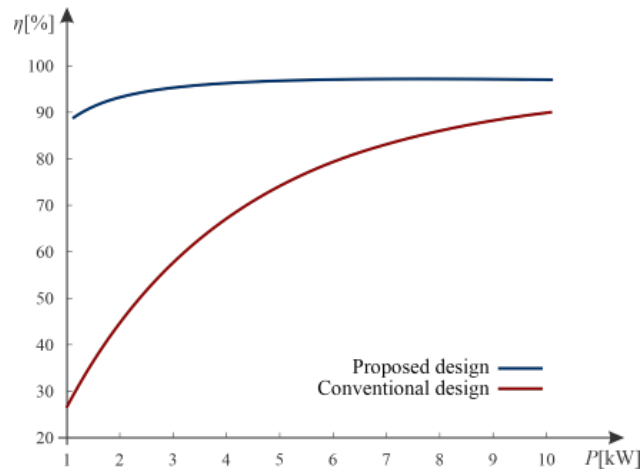
and smallest source is switching and conduction losses in the power stages of the QAB and H-bridge rectifier. Since ZVS of the QAB is already being employed, not much can be done to improve these losses further. The next largest source of loss is found to be the copper loss of the series inductance in the QAB. The largest source of loss is due to copper and core loss in the transformer. It is clear that improvements can be made in the magnetics to further enhance system efficiencies.

Figure 2.22: Efficiency and loss breakdown of a single module operating with ZVS at full voltage.

(a)

(b)
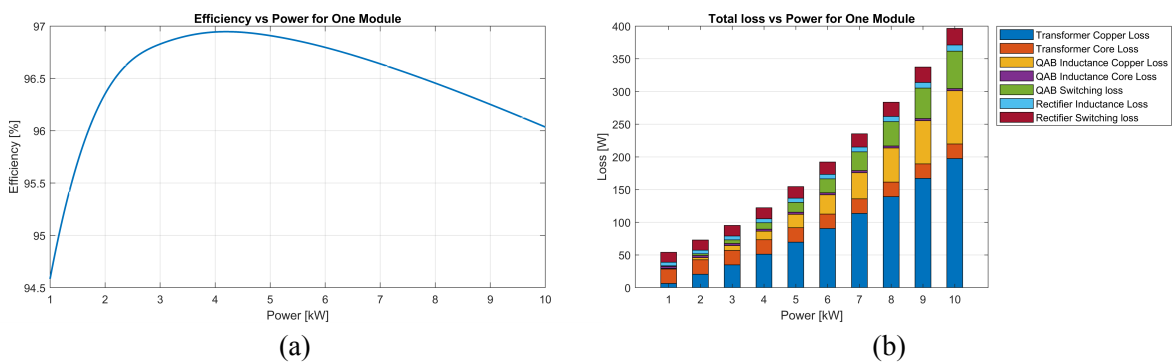
2.5   Conclusions

This chapter outlines a modular multi-stage three-phase ac-to-dc converter designed to balance three-phase power and eliminate twice-line frequency pulsating power from the dc-port. The bidirectional, modular, and scalable converter architecture is a promising solution for various applications such as PV string inverters, XFCs, and P2H systems. The architecture consists of N modules, each with flexible configurations of ac and dc ports to meet specific application requirements. The module contains a self-contained multi-stage three-phase ac-to-dc converter comprised of three H-bridge ac-to-dc converters and one QAB dc-to-dc converter. The QAB reduces power conversion stresses, improves converter efficiency, and enhances power density. Soft switching methods are used to improve efficiency within the module. The system also uses a distributed control scheme, allowing each module to be controlled independently. The design process of the H-bridge and QAB converters is detailed, from the selection of key components to the development of control loops for dc-link and current regulation. A P2H simulation example is presented and a $10\,\mathrm{kW}$ scaled prototype is developed to validate the modular approach.

Chapter 3

Conclusions and Future Work

3.1   Thesis Summary and Conclusions

This work has highlighted the urgent need for a shift towards electrified transportation to mitigate the effects of climate change. By comparing electric vehicles (EVs) and internal combustion engine (ICE) technologies, it was demonstrated that EVs have significant advantages in terms of lower greenhouse gas emissions, energy efficiency, and reduced operating costs. However, it was also noted that EVs face certain impediments to adoption, including higher upfront costs due to batteries, limited range, and inadequate charging infrastructure. There is a need for continued research and development of EV technologies to address these impediments and make EVs a more attractive option for consumers. In addition, steps must be taken to expand the charging infrastructure and renewable energy generation to power these vehicles.

One potential solution to some of the the challenges facing widespread adoption is extreme fast charging (XFC) technology. The implementation of XFC has the potential to greatly reduce charging times and increase the convenience of EVs for consumers. Furthermore, this technology can help alleviate concerns regarding limited vehicle range and the need for more widespread charging infrastructure. An overview of current trends in EV charging technology reliant on conventional MVAC-to-DC system architectures is presented. These architectures present opportunities for improvement by removing the bulky low-frequency (LF) transformer and low-voltage (LV) bus wiring. Modular system architectures have been identified as a potential solution that eliminates these components, improving overall efficiencies and footprint of EV charging systems.

A potential modular architecture for EV charging is presented in Chapter 2. The design of the converter power stages through passive component selection and control loop design was discussed. A power-to-hydrogen (P2H) simulation example comprised of 18 ISOP modules was also developed to validate the module and system-level architecture and control. Tests were then performed on a scaled 10 kW prototype to verify operation of the power stage and controls as well as the bidirectional capability and scalability of the system in hardware. The results of these tests demonstrate the potential for modular architectures to provide a more efficient and compact solution for EV charging and P2H systems. As EV technology continues to improve and become more widely adopted, the development of modular architectures will be crucial in ensuring that charging infrastructure can keep pace with growing demand.

In conclusion, this thesis highlights the ongoing shift towards electrified transportation to reduce the effects of climate change and the challenges facing EV adoption. Through the comparison of EV and ICE technologies, impediments to EV adoption, and potential solutions such as XFC and modular architectures, this thesis provides valuable insights into the future of transportation. The power-to-hydrogen system example presented in this thesis also demonstrates the feasibility and potential of modular architectures to address these challenges and contribute to a more sustainable future for transportation.

3.2   Future Directions

Future research directions based on the findings of this thesis can include further development of PV inverter system integration, with a focus on debugging inverter firmware and running tests at full medium voltage ac (MVAC), as well as running grid-forming and grid-following tests with the modular inverter architecture. Additionally, research can continue in the areas of XFC and P2H system designs, including three-phase rectifier tests and testing multiple series-connected modules in rectifier operation, as well as making improvements to system efficiency and transformer design.

Further research can also explore a more detailed comparison of modular system cost, efficiency, and energy density as compared to traditional LF-based MVAC-to-DC systems. This

could help to better understand the potential benefits of modular architectures and inform future development and implementation efforts.

Bibliography

[1] A Day in the Life of Your Car (and its Associated Emissions).

[2] During 2021, u.s. retail electricity prices rose at fastest rate since 2008.

[3] Electric vehicles have a weight problem - fast company.

[4] Find and Compare Cars.

[5] Gasoline explained - factors affecting gasoline prices.

[6] Lineup of VW passenger vehicles.

[7] Short-term energy outlook - electricity.

[8] This ev charger map shows how climate change's infrastructure problem.

[9] U.s. energy information administration - eia - independent statistics and analysis.

[10] U.s. energy information administration - eia - independent statistics and analysis.

[11] Weekly retail gasoline and diesel prices.

[12] Lithium-ion battery pack prices rise for first time to an average of $151/kwh, Dec 2022.

[13] Prasanta K. Achanta, Brian B. Johnson, Gab-Su Seo, and Dragan Maksimovic. A multilevel dc to three-phase ac architecture for photovoltaic power plants. IEEE Transactions on Energy Conversion, 34(1):181–190, 2019.

[14] U.S. Energy Information Administration. Electricity in the united states. `https://www.eia.gov/energyexplained/electricity/electricity-in-the-us.php`, 2021.

[15] Adnan Ahmad, Zian Qin, Thiwanka Wijekoon, and Pavol Bauer. An overview on medium voltage grid integration of ultra-fast charging stations: Current status and future trends. IEEE Open Journal of the Industrial Electronics Society, 2022.

[16] Aiman Albatayneh, Mohammad N Assaf, Dariusz Alterman, and Mustafa Jaradat. Comparison of the overall energy efficiency for internal combustion engine vehicles and electric vehicles. Rigas Tehniskas Universitates Zinatniskie Raksti, 24(1):669–680, 2020.

[17] Jeff S. Bartlett and Ben Preston. Automakers are adding electric vehicles to lineups.

[18] Aaron Brooker, Alicia Birky, Evan Reznicek, Jeff Gonder, Chad Hunter, Jason Lustbader, Chen Zhang, Lauren Sittler, Arthur Yip, Fan Yang, et al. Vehicle technologies and hydrogen and fuel cell technologies research and development programs benefits assessment report for 2020. Technical report, National Renewable Energy Lab.(NREL), Golden, CO (United States), 2021.

[19] Alternative Fuels Data Center. Electric vehicle emissions, Accessed 2023.

[20] Mengxing Chen, Shih-Feng Chou, Frede Blaabjerg, and Pooya Davari. Overview of power electronic converter topologies enabling large-scale hydrogen production via water electrolysis. Applied Sciences, 12(4), 2022.

[21] Levy F. Costa, Giampaolo Buticchi, and Marco Liserre. Modular smart transformer architectures: An overview and proposal of a interphase architecture. pages 1–7, 2017.

[22] David Cullen. 3 critical challenges to electrifying america's truck fleet, Dec 2022.

[23] Rik WAA De Doncker, Deepakraj M Divan, and Mustansir H Kheraluwala. A three-phase soft-switched high-power-density dc/dc converter for high-power applications. IEEE transactions on industry applications, 27(1):63–73, 1991.

[24] Soham Dutta, Branko Majmunovic, Satyaki Mukherjee, Rahul Mallik, Gab-Su Seo, Dragan Maksimovic, and Brian Johnson. A novel decentralized pwm interleaving technique for ripple minimization in series-stacked dc-dc converters. In 2021 IEEE Applied Power Electronics Conference and Exposition (APEC), pages 487–493. IEEE, 2021.

[25] Robert W Erickson and Dragan Maksimovic. Fundamentals of power electronics. Springer, 3rd edition, 2020.

[26] Evatran. 32 different ev models can do 100% electric daily driving: Infographic from plugless power.

[27] Felix Hoffmann, Luis Camurca, and Marco Liserre. Modular EV fast charging station architectures based on multiphase-medium-frequency transformer. pages 1327–1332, 2018.

[28] J. E. Huber and J. W. Kolar. Solid-state transformers: on the origins and evolution of key concepts. IEEE Industrial Electronics Magazine, 10(3):19–28, 2016.

[29] Iea. Global ev outlook 2020 – analysis.

[30] Iea. Global ev outlook 2021 – analysis.

[31] Texas Instruments. Tms320f2837xd dual-core microcontrollers: Technical reference manual, 2019.

[32] Vishnu Mahadeva Iyer, Srinivas Gulur, Ghanshyamsinh Gohil, and Subhashish Bhattacharya. Extreme fast charging station architecture for electric vehicles with partial power processing. pages 659–665, 2018.

[33] Gautam Kalghatgi. Is it really the end of internal combustion engines and petroleum in transport? Applied energy, 225:965–974, 2018.

[34] M.N. Kheraluwala, R.W. Gascoigne, D.M. Divan, and E.D. Baumann. Performance characterization of a high-power dual active bridge dc-to-dc converter. IEEE Transactions on Industry Applications, 28(6):1294–1301, 1992.

[35] Z Liu and RA Dougal. A review of electric vehicle charging infrastructure deployment in smart grid environment. IEEE Transactions on Smart Grid, 1(1):45–52, 2006.

[36] Branko Majmunović. Optimization of Active-Bridge Based Modular Power Converters. PhD thesis, University of Colorado at Boulder, 2022.

[37] Branko Majmunovic, Satyaki Mukherjee, Trent Martin, Rahul Mallik, Soham Dutta, Gab-Su Seo, Brian Johnson, and Dragan Maksimovic. 1 kV, 10 kW SiC-based quadruple active bridge DCX stage in a dc to three-phase ac module for medium-voltage grid integration. IEEE Transactions on Power Electronics, pages 1–17, 2022.

[38] M. Muratori. Impact of uncoordinated plug-in electric vehicle charging on residential power demand. Nat Energy, 3:193–201, 2018.

[39] Union of Concerned Scientists. Cleaner cars from cradle to grave: How electric cars beat gasoline cars on lifetime global warming emissions. Technical report, Union of Concerned Scientists, 4 2015.

[40] U.S. Department of Energy. Alternative Fuels Data Center: Fuel Properties Comparison. https://afdc.energy.gov/fuels/properties, Accessed: April 22, 2023.

[41] ScienceDirect. Regenerative braking. https://www.sciencedirect.com/topics/engineering/regenerative-braking, 2021. Accessed: April 23, 2023.

[42] Hao Tu, Hao Feng, Srdjan Srdic, and Srdjan Lukic. Extreme fast charging of electric vehicles: A technology overview. IEEE Transactions on Transportation Electrification, 5(4):861–878, 2019.

[43] Huanhuan Zhang, Zhengguang Zou, Shuchao Zhang, Jie Liu, and Shenglin Zhong. A review of the doping modification of lifepo4 as a cathode material for lithium ion batteries. Int. J. Electrochem. Sci, 15:12041–12067, 2020.